applied sciences

MDPI

Article

Process Analysis, Characterization and Multi-Response Optimization of Double-Walled WAAM Aluminum Alloy Structures

Jure Krolo [1,*], Aleš Nagode [2], Ivan Peko [3] and Ivana Dumanić Labetić [1]

[1] Faculty of Electrical Engineering, Mechanical Engineering and Naval Architecture, University of Split, Ruđera Boškovića 32, 21000 Split, Croatia; iduman00@fesb.hr
[2] Faculty of Natural Sciences and Engineering, University of Ljubljana, Aškerčeva 12, 1000 Ljubljana, Slovenia; ales.nagode@ntf.uni-lj.si
[3] Faculty of Science, University of Split, Ruđera Boškovića 33, 21000 Split, Croatia; ipeko@pmfst.hr
* Correspondence: jkrolo@fesb.hr

Abstract

The main aim of this study was to evaluate the applicability of a low-cost, double-wall gas metal arc welding (GMAW)-based wire arc additive manufacturing (WAAM) process for aluminum alloy AlMg5, with an emphasis on microstructural heterogeneity, layer-dependent defect formation, and their implications for mechanical performance and geometric characteristics. A Taguchi L9 (3^3) design of experiments was employed to investigate the influence of welding current (40–60 A), shielding gas flow (10–20 L/min), and arc correction (0–40%) on wall geometry, material utilization, and overall process quality through multi-response optimization. The optimal parameter set (60 A, 15 L/min, 0% arc correction) resulted in a 54.9% improvement in the Grey Relational Grade compared to the lowest-performing configuration. Metallographic analysis revealed heterogeneous grain evolution governed by the multilayer thermal history, with porosity levels ranging from 3.20% to 3.49% and lack-of-fusion defects preferentially concentrated in interlayer and mid-height regions. The fabricated high-wall structure exhibited hardness values between 72 and 85 HV and an average ultimate tensile strength of 175 MPa. The observed mechanical scatter was consistent with localized microstructural heterogeneity and spatial defect distribution. The results demonstrate that geometric evaluation alone is insufficient as a quality metric for WAAM components and must be complemented by metallographic integrity assessment. Overall, the study highlights the importance of direct parameter optimization in double-wall WAAM structures to mitigate defect formation and enhance mechanical reliability under industrially accessible deposition conditions.

Keywords: wire arc additive manufacturing (WAAM); gas metal arc welding (GMAW); aluminum alloy; double-wall deposition; Taguchi method; microstructural characterization

Check for updates

Academic Editor: Nthabiseng Maledi

Received: 27 January 2026
Revised: 18 February 2026
Accepted: 24 February 2026
Published: 26 February 2026

Copyright: © 2026 by the authors. Licensee MDPI, Basel, Switzerland. This article is an open access article distributed under the terms and conditions of the Creative Commons Attribution (CC BY) license.

1. Introduction

Wire arc additive manufacturing (WAAM) is a metal additive manufacturing technology belonging to the Directed Energy Deposition (DED) family, in which metallic wire is continuously fed into a melt pool generated by an electric arc heat source. Material is deposited layer by layer following a predefined digital toolpath, enabling the production of near-net-shape components with medium to large dimensions. Compared to powder-based additive manufacturing processes, WAAM is characterized by significantly higher

deposition rates, reduced material waste, and lower feedstock costs, making it particularly attractive for large-scale structural applications [1–4].

In WAAM, several arc welding processes can be employed as heat sources, including gas metal arc welding (GMAW), gas tungsten arc welding (GTAW), plasma arc welding (PAW), and cold metal transfer (CMT). Among these, GMAW-based WAAM is widely used due to its robustness, high productivity, and compatibility with aluminum alloys. The use of wire as feedstock also provides advantages in terms of material cleanliness, handling safety, and chemical composition control when compared to powder-based systems [5,6]. Most of the more relevant engineering alloys (titanium, aluminum, and steels, including stainless steel) are already used in WAAM with excellent results, proving the viability of this technique to produce custom-made large metallic parts [7]. Furthermore, recent studies have highlighted the growing interest in WAAM of aluminum alloys, particularly for large-scale structural applications. Aluminum alloys are of particular interest in wire arc additive manufacturing due to their high strength-to-weight ratio, corrosion resistance, and widespread use in aerospace, marine, and transportation industries. However, the WAAM of aluminum alloys is associated with specific challenges, including high thermal conductivity, susceptibility to porosity, oxide formation, and distortion caused by heat accumulation during multi-layer deposition, as reported in previous studies [7,8]. Langelandsvik et al. provided a comprehensive review of aluminum alloy development for WAAM, emphasizing the critical role of alloy composition and process conditions in controlling porosity, residual stresses, and solidification cracking. Their work underlines the strong interdependence between process parameters, alloy chemistry, and resulting microstructure, forming the basis for further optimization of aluminum WAAM technologies [8]. Furthermore, the thermal history inherent to WAAM strongly influences bead geometry, interlayer bonding, microstructural evolution, and mechanical performance. Repeated thermal cycling during layer-by-layer deposition typically leads to columnar grain growth along the build direction, microstructural anisotropy, and spatial variations in hardness and strength. As a result, increasing research attention has been devoted to understanding structure and property relationships in WAAM-fabricated aluminum components [9,10]. Garašić et al. investigated the mechanical and microstructural properties of WAAM produced walls made from Al–Mg–Si alloy 6063 using AC and DC MIG processes. Their results demonstrated that the balance of AC polarity influences wall geometry, porosity, grain structure, and residual stress distribution. Higher electrode-negative ratios promoted taller and narrower walls with reduced porosity and a refined, predominantly equiaxed grain structure, while DC MIG deposition resulted in higher residual stress levels. The study confirmed that appropriate control of welding current type and polarity balance is essential for achieving stable mechanical performance and minimizing process-related defects in aluminum WAAM structures [9]. Yu et al. investigated the microstructure and mechanical properties of an Al–Zn–Mg–Cu alloy fabricated by wire arc additive manufacturing using in situ alloying with multiple heterogeneous wires. Their results showed a characteristic layered microstructure, with columnar grains dominating the lower part of each deposited layer and equiaxed grains forming in the upper region due to local thermal gradients and solidification conditions. The WAAM fabricated alloy exhibited pronounced anisotropy in mechanical properties, with significantly higher tensile strength in the horizontal direction compared to the build direction, which was attributed to grain morphology and the presence of interlayer pores and microcracks [10]. Gierth et al. systematically investigated WAAM of the AlMg5Mn aluminum alloy using GMAW-based CMT and its advanced variants. Their results showed that reducing heat input through polarity-controlled CMT-ADV and CMT-PADV arc modes significantly decreases porosity, refines grain structure, and improves geometric accuracy. In particular, the CMT-PADV

process achieved the lowest porosity and near-isotropic mechanical properties, highlighting the strong coupling between energy input, thermal history, and microstructural evolution in aluminum WAAM [11]. Feng et al. examined bead formation and microstructure evolution in the CMT- and pulsed CMT-based WAAM of 316 stainless steel. They demonstrated that the use of a pulsed CMT arc expands the stable process window, enables higher travel speeds, and leads to significant grain refinement compared to conventional CMT. Their analysis confirmed a reduction in average grain size and a more randomized grain orientation when using pulsed CMT, underlining the effectiveness of pulse controlled heat input for microstructural control in WAAM [2].

In contrast, the present study addresses the direct optimization of a cost-effective, double-wall synergic GMAW-based WAAM process, integrating geometric efficiency indicators (*MU*, *SI*, *EUWA*, and LoF) with microstructural and mechanical characterization in a unified Taguchi–GRA framework. This approach enables simultaneous control of geometric accuracy, defect formation, and structural reliability under industrially accessible deposition conditions.

A recent critical review analyzed the role of different CMT arc variants in improving the quality of aluminum alloy components produced by WAAM [12]. CMT-based deposition, owing to its reduced heat input and controlled metal transfer, was shown to decrease residual stresses, distortion, and porosity while improving surface finish and dimensional accuracy. Advanced variants such as CMT-Pulse and CMT-Advanced further refine grain structure and enhance mechanical performance. Akhavan Malayeri et al. investigated heterogeneous microstructure and mechanical behaviour in WAAM-fabricated Al–2219 alloy, reporting alternating equiaxed and columnar grain regions that enabled a favourable strength–ductility combination, further improved after T6 heat treatment [13]. Similar improvements in hardness and tensile strength after heat treatment were reported for the WAAM 2319 alloy [14]. Ren et al. demonstrated that solution treatment and ageing in the WAAM-fabricated 2319 Al–Cu alloy modify second-phase morphology and increase microhardness, although ageing may increase fine porosity and reduce corrosion resistance [15]. Recent studies have primarily focused on CMT-based systems and post-deposition heat treatment strategies for aluminum WAAM, whereas comparatively limited attention has been devoted to the direct optimization of multi-pass or multi-wall deposition under cost-effective synergic GMAW configurations. Wang et al. systematically investigated the influence of arc torch angle on deposition behaviour, thermal distribution, microstructure, and mechanical properties in GMAW-based WAAM of a ZL205A aluminum alloy. By varying the torch angle from 60° to 120°, they demonstrated that changes in heat input distribution strongly affect molten pool stability, droplet transfer behaviour, layer penetration, and porosity formation. The formation accuracy on the sidewall surface was increased when the torch angle increased to 100–120°, with the reduced surface roughness Sa varying from 88 μm to 121 μm. The reduced porosity was determined with a slightly inclined obtuse torch angle of 100°. At this torch angle, the elongation and tensile strength reached maximum values of 17.1% and 258.6 MPa, respectively [16]. Recent studies have increasingly focused on modelling and optimization of the process parameters in wire arc additive manufacturing. Dinovitzer et al. investigated the influence of TIG-based WAAM process parameters on bead geometry and microstructure of Hastelloy X. The Taguchi experimental design combined with analysis of variance (ANOVA) was applied to identify the relationships between process parameters and the resulting responses [17]. A direct linear relationship was observed between wire feed rate and bead height, while no noticeable influence of wire feed rate was detected on melt-through depth or surface roughness. Increasing travel speed or decreasing welding current reduces heat input, leading to decreased bead width and melt-through depth but increased surface rough-

ness, while argon flow rate has no statistically significant influence on bead geometry or surface quality. Kumar and Anandakrishnan concluded that wire feed speed is the most influential parameter affecting weld bead width in a MIG-based WAAM process of Inconel 825, followed by voltage and welding speed [18]. Taguchi L9 orthogonal array and ANOVA were used to determine the optimal combinations of parameters for achieving the highest bead width (0.25 m/min weld velocity, 8 m/min wire feed speed, and 28 V voltage). Naveen Srinivas et al. examined the influence of process parameters in wire arc additive manufacturing of 5356 aluminum alloy [19]. Optimal process parameters were identified by using the Taguchi method and Grey Relational Analysis. Wire feed rate, gas flow rate, and welding speed were considered as input parameters, while bead geometry and width, fabrication time, and porosity features were evaluated as responses. Yang et al. focused on the optimization of T6 heat-treatment parameters of a WAAM-fabricated 2219 aluminum alloy (Al–Cu) using a Taguchi experimental design [20]. Solution temperature was identified as the most significant factor affecting ultimate tensile strength and yield strength, while ageing time had the greatest effect on elongation. The results showed that Taguchi-based experimental modelling is effective for improving the mechanical performance of WAAM aluminum alloys and achieving strength levels closer to wrought materials without relying on numerical simulations. Kumar and Maji developed response surface models for predicting bead width, bead height, and cross-sectional area in WAAM using a Box–Behnken experimental design [21]. Voltage, wire feed rate, travel speed, and gas flow rate were identified as significant factors for the deposition of 304L stainless steel. A genetic algorithm (GA) was employed to obtain optimal parameter combinations to minimize voids and excess material. The mechanical and metallurgical properties of the fabricated multi-bead slice were found to be comparable to those of the feedstock wire (yield strength 335.50 MPa, ultimate tensile strength 543.75 MPa, percentage elongation 68.25%, and the average Vickers micro-hardness 186.82 HV). On the other hand, peak current was found to be the most dominant input parameter for bead width and height, by applying advanced evolutionary algorithms [22]. Xia et al. developed machine learning models, including an adaptive neuro-fuzzy inference system (ANFIS) model optimized by GA, to predict surface roughness in WAAM of mild carbon steel ER70S-6 [23]. The study confirmed that a structured design of experiments (DOE) is essential for producing high-quality training data. The same material was used in the TIG-based WAAM process [24]. The optimization of input parameters (current, voltage, and travel speed) was made using the response surface method, and the properties were validated by experimentation. Wacker et al. [25] applied enhanced artificial neural networks (ANNs) to predict the distortion for multi-layer WAAM structures of 15NiCr13 steel. The authors emphasized that low error between the predicted and measured distortion was achieved, i.e., very good results have been achieved even in comparison to other publications. Irfan et al. proposed a hybrid modelling framework combining DOE, response surface methodology and ANN to optimize bead geometry and deposition efficiency in the WAAM process using AISI 630 stainless steel [26]. The authors confirmed the importance of DOE-based data collection. Similar conclusions were reported for VAC 60 alloy [27].

To enable broader industrial applicability, a double-wall (double-pass) WAAM deposition strategy combined with Taguchi-based parameter optimization was investigated in this study. A Taguchi L9 (3^3) design of experiments was employed to analyze the effects of welding current, shielding gas flow, and arc correction on wall geometry, material utilization, and overall process quality through multi-response optimization. While most existing WAAM optimization studies focus on single-bead deposition, such bead-level optimization does not necessarily translate to multi-bead or double-wall structures, where overlapping passes and cumulative thermal effects strongly influence internal bonding,

defect formation, and microstructural evolution. However, in multi-bead and double-wall WAAM structures, overlapping passes and repeated thermal cycling fundamentally alter local heat accumulation, interlayer bonding, and defect formation mechanisms, making direct extrapolation from single-bead optimization insufficient. These effects are particularly pronounced in aluminum alloy WAAM. The influence of process parameter optimization applied directly to double-wall deposition strategies, especially in GMAW-based WAAM of aluminum alloys, remains insufficiently explored. To address this research gap, following Taguchi–GRA multi-response optimization, only the parameter set identified as optimal was employed to fabricate a high-height double-wall WAAM structure for detailed mechanical testing and comprehensive metallographic analysis.

2. Materials and Methods

Wire arc additive manufacturing was conducted using a gas metal arc welding system. A Daihen Varstroj WB-P500L welding power source (Varstroj, Lendava, Slovenia) was employed for all deposition experiments. The welding torch was operated in a mechanized setup with controlled motion to ensure stable and repeatable deposition conditions. In this research, a low-cost WAAM setup was developed by integrating a commercially available polymer-based 3D printer motion system (3-axis gantry) named 3D FORCEBOOK – UltraPrint 3D (HGSPOT Grupa d.o.o., Zagreb, Croatia) with the GMAW device described above. This approach demonstrates the potential for retrofitting and adapting existing additive manufacturing platforms for metal WAAM applications without the need for dedicated or proprietary WAAM systems. The Ultimaker Cura 5.8.1 software was employed to slice the 3D model and generate deposition paths, which were subsequently modified to be compatible with the GMAW system; see Figure 1. Due to limitations in synchronizing arc ignition and extinction with the printer control system, arc start and stop operations were performed manually, highlighting both the flexibility and current constraints of such low-cost WAAM configurations. This limitation could be overcome in future configurations by implementing digital I/O synchronization between the motion controller and the welding power source, enabling automated arc ignition and termination aligned with programmed toolpaths. Alternatively, integration of an external trigger interface or microcontroller-based coupling could provide basic start/stop synchronization without requiring full closed-loop process control. The gantry motion system was used purely as an XYZ positioning unit executing G-code toolpaths, without any electronic coupling to the welding power source. The Ultimaker Cura-generated toolpaths were post-processed to match the required deposition kinematics (travel speed, path ordering, and fixed Z-increment) and to remove polymer-printing-specific commands not relevant to WAAM. Welding parameters were governed by the synergic program of the GMAW power source (current level/arc correction), while the gantry provided repeatable motion for all experimental runs. However, for the fabrication of double-wall WAAM wall structures, the proposed process demonstrated sufficient functionality for experimental investigation.

In this research, aluminum walls were deposited using a double-wall deposition strategy, introducing a deposition route that differs from the majority of previously reported WAAM studies [3,17]. Compared to conventional single-bead WAAM wall fabrication, the proposed double-wall, bidirectional deposition strategy offers several potential advantages. The forward–reverse deposition path can promote a more balanced heat distribution within each layer, which may reduce thermal gradients and associated geometric instabilities. Deposition strategy has been shown in previous investigations to significantly influence melt pool stability, heat distribution, geometric stability, porosity evolution, and the resulting mechanical response in WAAM-fabricated components [28,29]. Applying two consecutive passes at the same layer height without intermediate cooling can enhance local remelting,

potentially improving inter-bead bonding and reducing the likelihood of lack-of-fusion defects. Additionally, the lateral offset between passes may contribute to improved material consolidation in the central region of the wall, which could help mitigate porosity formation commonly observed in single-bead walls. Overall, this deposition approach represents a simple modification of the conventional WAAM process that may improve geometric consistency and internal integrity without requiring additional equipment, but also simulate possible real application of multibead WAAM wall deposition. Therefore, the objective of this approach was to investigate the influence of such a deposition methodology on the geometric characteristics and resulting properties of the fabricated walls. The deposition device was programmed to move in a single direction to produce a bead with a constant width of 5 mm, followed by a reverse movement with a 5 mm lateral offset, thereby forming a bidirectional (forward–backward) deposition path and double-layered WAAM walls. The total travel length for each pass was maintained at 85 mm; see Figure 1. Before wall fabrication, the single-bead width and height were experimentally measured for a selected range of parameters. Based on these measurements, the *Z*-axis increment between successive layers was defined and fixed at 2.5 mm, ensuring stable layer stacking and consistent wall geometry. To mitigate the risk of porosity formation, particularly in the central region of the WAAM wall, two consecutive single-level passes were applied without intermediate cooling. After completing these two passes (four travels or paths), the specimens were cooled from the substrate side in water to room temperature before the deposition of subsequent layers. Overall, the adopted methodology can be summarized as follows: forward deposition, reverse deposition with a lateral offset of 5 mm selected based on preliminary bead width measurements to ensure controlled inter-pass overlap, vertical displacement of 2.5 mm along the *Z*-axis, repetition of the forward–reverse sequence, followed by controlled cooling to ambient temperature. The *Z*-axis increment was kept constant for all parameter combinations in order to maintain comparability within the Taguchi experimental design and to avoid introducing an additional process variable.

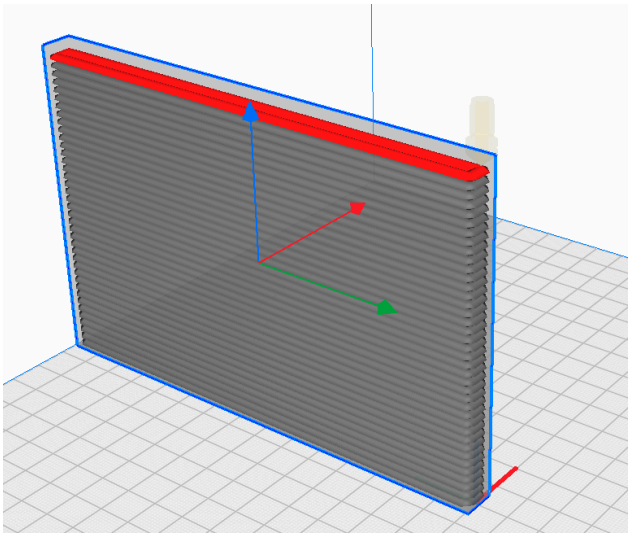


Figure 1. Schematic presentation of slicing and 3D printing methodology for double-layered aluminum WAAM wall.

In order to determine the influence of the welding current, gas flow, and arc correction Taguchi L9 experimental plan was employed to obtain 9 different deposited Al double-layered walls (i.e., double walls); see Table 1. In addition to welding current and shielding gas flow, arc stability was explicitly controlled through the arc correction parameter provided by the GMAW power source. Arc correction (%) represents a synergic

control parameter of the GMAW power source that adjusts the arc length and metal transfer behaviour relative to the nominal synergic setting. By modifying the arc voltage–current relationship, arc correction influences arc stability, droplet transfer, and heat input distribution during deposition. It should be noted that arc correction represents a machine-specific synergic control parameter defined by the internal algorithm of the employed welding power source. Therefore, the quantitative effects reported in this study are directly linked to the used equipment and its control logic. Nevertheless, the general influence of arc stability and arc length control on deposition quality is expected to be applicable to other synergic GMAW systems. The welding experiments were conducted in synergic pulsed GMAW mode, resulting in a pulsed spray metal transfer regime. In this operating configuration, the arc voltage, peak current, base current, pulse frequency, and waveform characteristics were automatically controlled by the power source according to the predefined synergic programme and the selected current level. Consequently, these parameters were not independently adjusted or recorded during the experiments. The contact tip-to-work distance (CTWD) was maintained constant at 15 mm throughout all depositions in order to ensure stable arc behaviour and consistent heat input conditions. Following Taguchi–GRA multi-response optimization, only the parameter set identified as optimal was employed to fabricate a high-height double-wall WAAM structure for detailed mechanical testing and comprehensive metallographic analysis.

Table 1. Taguchi L9 (3^3) experimental plan and input parameters for WAAM deposition.

Exp.	Arc Correction (%)	Current (A)	Gas Flow (L/min)
1	40	40	10
2	40	50	15
3	40	60	20
4	20	40	15
5	20	50	20
6	20	60	10
7	0	40	20
8	0	50	10
9	0	60	15

In order to reduce experimental time, 5 double passes (10 deposited double wall layers in total), as described above, were employed in order to save time and resources. Output parameters, surface irregularity, material utilization, effective usable wall area, porosity, and surface roughness were measured, respectively. Due to the synergic control of voltage and pulse waveform parameters, the effective arc heat input was not explicitly calculated in this study. The nominal welding current was therefore treated as the primary controllable parameter governing the relative heat input within the investigated experimental domain. The parameters that were held constant, along with the deposition device moving, are given in Table 2.

Table 2. Welding parameters used for WAAM walls deposition.

WAAM Deposition Parameters			
Electric current (A)	40, 50, 60	**Electrode type**	ϕ 1.2 mm aluminum
Work mode	DCEP	**Filler material**	AlMg5 (5356)
Pulse welding	yes	**Moving speed (cm/min)**	34.26
Protective gas	Argon 100%	***Z*-axis movement**	2.5 mm
Arc correction (%)	0, 20, 40	**CTDW (mm)**	15
Gas flow (L/min)	10, 15, 20	**Interpass temperature**	room

Surface irregularity (*SI*) and material utilization (*MU*) were employed as quantitative parameters for the assessment of the geometric quality and process efficiency of the WAAM-fabricated wall structures, and they are defined with Equations (1) and (2) as follows [11]:

$$SI = \frac{(MWW - EWW)}{2} \quad (1)$$

$$MU = \frac{EUWA}{(EUWA + a + b)} \quad (2)$$

Surface irregularity characterizes the lateral surface waviness of the deposited walls and is defined as half of the difference between the maximum wall width (*MWW*) and the effective wall width (*EWW*), as schematically illustrated in Figure 2. This parameter reflects the deviation of the actual wall contour from the effectively usable geometry and is therefore directly related to the extent of material that must be removed during post-processing operations such as machining or milling. Material utilization represents the efficiency of material usage in the additive manufacturing process and is defined as the ratio of the effective usable wall area (*EUWA*) to the total deposited wall area, excluding the unavoidable base material; see Figure 2. In practical applications, areas a, b, and c, also shown in Figure 2, are typically removed after additive manufacturing in order to obtain the final functional geometry. However, as suggested by Gierth et al. [11], area c is not considered in the calculation of material utilization in this study, since it occurs regardless of the number of deposited layers and must be removed subtractively in all cases. Consequently, this area has a more pronounced influence when a small number of welded layers is present, while its relative contribution decreases as the number of deposited layers increases [11].

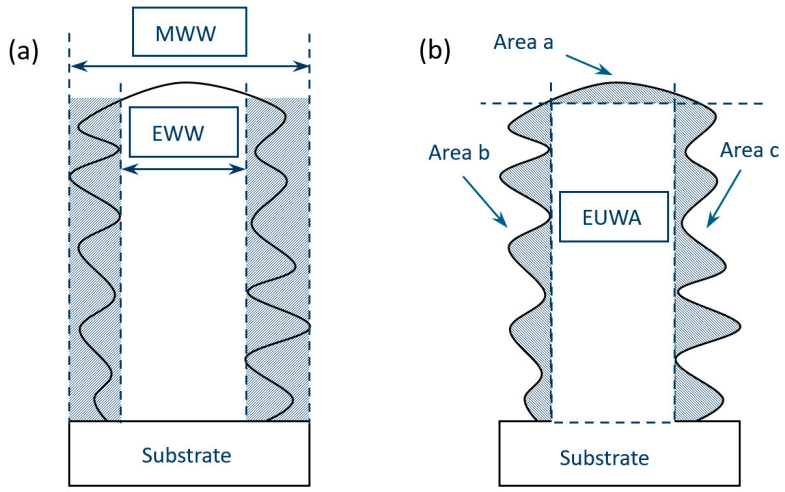


Figure 2. Simplified schematic representation of the characteristic geometry of the deposited WAAM wall: (**a**) maximum wall width (*MWW*) and effective wall width (*EWW*); (**b**) effective usable wall area (*EUWA*).

Higher material utilization values indicate near-net-shape manufacturing with reduced material waste and lower post-processing requirements, whereas lower values imply less efficient material usage and increased machining effort. Together, SI and *MU* provide complementary insight into both the geometric accuracy and the process efficiency of the WAAM deposition strategy employed in this work. Furthermore, the porosity within the effective usable wall area (*EUWA*) was evaluated in order to assess the quality of the material that remains after post-processing. Porosity within *EUWA* was defined as the ratio of the total pore area (or lack of fusion areas) located inside the *EUWA* to the *EUWA* itself.

After WAAM deposition, specimens were cut from each deposited wall using a Buehler Delta Abrasimet metallographic cutter (Buehler, Lake Bluff, IL, USA). The specimens were subsequently ground and polished using a Struers Labopol-Z metallographic polishing system (Struers, Ballerup, Denmark). Grinding was performed using 1200 grit SiC paper, followed by a one-stage polishing with 9 µm alumina for Taguchi geometry characterization and a four-stage polishing procedure, with final polishing carried out using a 0.03 µm colloidal silica suspension for macro and microstructure analysis. Grinding and polishing were continued until a metallic gloss surface was achieved; however, residual porosity remained visible on the prepared surfaces. For the optical microscopy, the samples were etched electrolytically with Barker's reagent (2.5% HBF4 in water) at 23 V for 1 min. Optical microscopy was performed utilizing an Olympus BX61 digital microscope (Olympus, Tokyo, Japan). The sample macrostructure geometry was characterized using an Olympus SZ61 optical stereomicroscope (Olympus, Tokyo, Japan). Digital images of the prepared specimens were analyzed using the open-source software ImageJ 1.54p (National Institutes of Health, Bethesda, MD, USA). Profilm3D optical 3D profilometer (KLA Corporation, Milpitas, CA, USA) was used as the technique of non-contact 3D profilometer analysis to measure surface roughness on top of the WAAM walls in the area 4 mm × 0.8 mm. The Profilm3D optical profiler uses white light interferometry, which enables the measurement of the surface profiles and roughness down to 0.05 µm. After multicriteria Taguchi-based optimization, one selected set of the parameters was employed to deposit an 85 mm in height aluminum double-layered wall for further characterization of mechanical properties and metallography analysis. Figure 3 shows the experimental setup for WAAM walls deposition and a schematic presentation of the used methodology and workflow in this research.

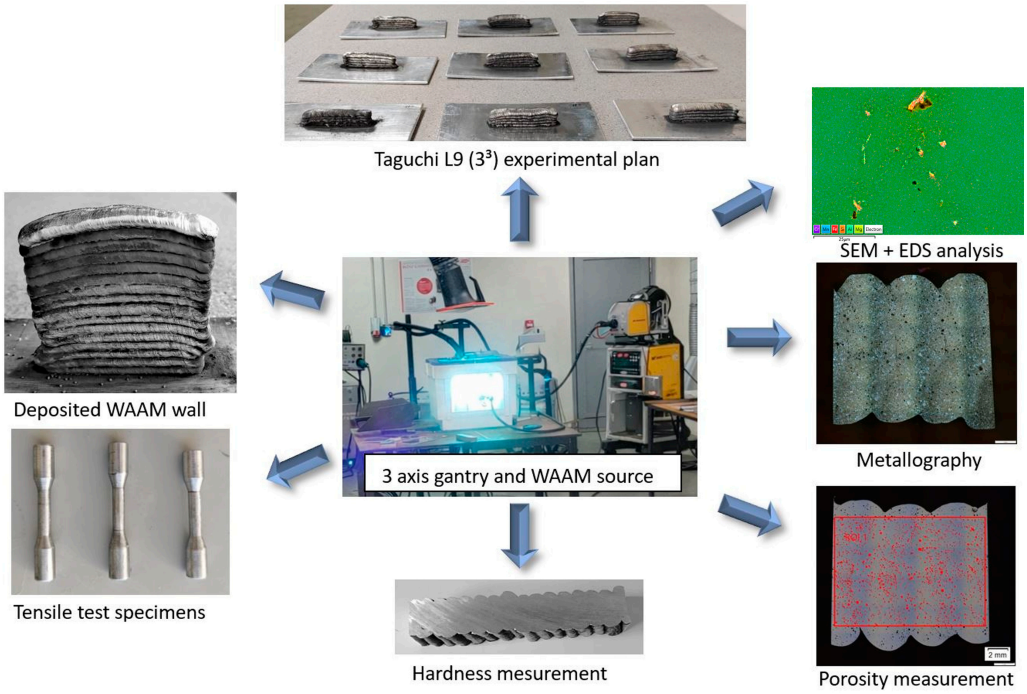


Figure 3. Schematic representation of the research flow diagram for the WAAM process procedure and the performed analysis.

For the WAAM process, an AlMg5 (ER5356) aluminum alloy wire was used as the filler material. The wire represents a general-purpose aluminum welding alloy. Its nominal chemical composition was as follows (wt.%): Si ≤ 0.25, Fe ≤ 0.40, Cu ≤ 0.10, Mn 0.05–0.20, Mg 4.5–5.5, Cr 0.05–0.20, Zn ≤ 0.10, Ti 0.06–0.20, Be ≤ 0.0003, and Al balance. AlMg5

(ER5356) aluminum alloy wire is one of the most commonly used filler materials in arc-based welding [30]. Owing to its relatively high magnesium content, this alloy exhibits good weldability, stable arc behaviour, and a low susceptibility to solidification cracking, which makes it particularly suitable for GMAW-based WAAM applications. In addition, AlMg5 demonstrates good corrosion resistance, especially in marine and humid environments, and provides adequate strength in the as-deposited condition without the need for post-deposition heat treatments. The wire had a diameter of 1.2 mm and was continuously fed through the welding torch during deposition. The 100% Argon shielding gas was supplied throughout the process to protect the molten pool from atmospheric contamination.

WAAM structures were fabricated in a layer-by-layer manner following predefined deposition paths. The same welding equipment, wire type, and shielding conditions were maintained for all experiments, ensuring that any observed differences in geometry or material characteristics originated from the applied deposition strategy rather than from variations in equipment. Further characterization consisted of mechanical testing and metallography analysis. Specimens were machined from the WAAM wall according to the HR EN ISO 6892-1 standard [31]. A tensile test was performed on an ETM-250-S Raagen universal tensile test machine with a maximum force of 250 kN (Raagen, Ankara, Turkey). Tensile specimens had a reduced section length of 28 mm, fillet radius of 2.50 mm, and gauge width of 5 mm, Figure 3. Quasi-static tensile testing was performed at room temperature. Three tensile tests were performed, and the mean value was selected. Microhardness measurements were performed on a cross-section of the WAAM-deposited wall to evaluate the hardness distribution along the build height; see Figure 3. The used device was a Shimadzu HMV-2T (Shimadzu, Kyoto, Japan) universal machine with an integrated DynoLITE camera with DynoCapture 2.0 software for computer analysis. The microhardness measurements were conducted using a load of 9.8 N for a duration of 10 s at room temperature. The first indentation was positioned on the WAAM wall at a distance of 3.65 mm from the bottom of the wall, and subsequent measurements were taken at regular vertical intervals of 3.65 mm, resulting in a total of 19 measurement positions. This approach enabled the assessment of hardness variation from the lower to the upper regions of the deposited material. Scanning electron microscopy (SEM) combined with energy-dispersive X-ray spectroscopy (EDS) was used for microstructural characterization of the walls. The analyses were performed using a Thermo Scientific Quattro S field emission scanning electron microscope (FEG-SEM, Hillsboro, OR, USA) equipped with an Ultim Max 65 SSD EDS detector from Oxford Instruments and operated via the Aztec software platform (Abingdon, UK). The accelerating voltage during EDS analysis was set to 20 kV.

3. Results and Discussion

3.1. Taguchi and Multi-Response Optimization

Figure 4 shows nine WAAM double walls obtained following the parameters from Taguchi L9 (3^3) experimental plan given in Table 1. The cross-section for metallographic analysis was taken from the central region of the 85 mm long wall. Approximately 30 mm from each end was excluded to avoid potential boundary and edge effects, resulting in a 25 mm central segment used for analysis. The section was prepared perpendicular to the deposition direction. Each wall corresponds to a unique combination of process parameters. Visual inspection reveals noticeable differences in wall geometry, surface morphology, and internal defect distribution among the specimens. Variations in bead uniformity and surface waviness are observed, while some walls exhibit visible porosity and lack-of-fusion defects, particularly along the central regions. These differences indicate a strong influence of process parameter combinations on the stability of the WAAM process and the resulting wall quality.

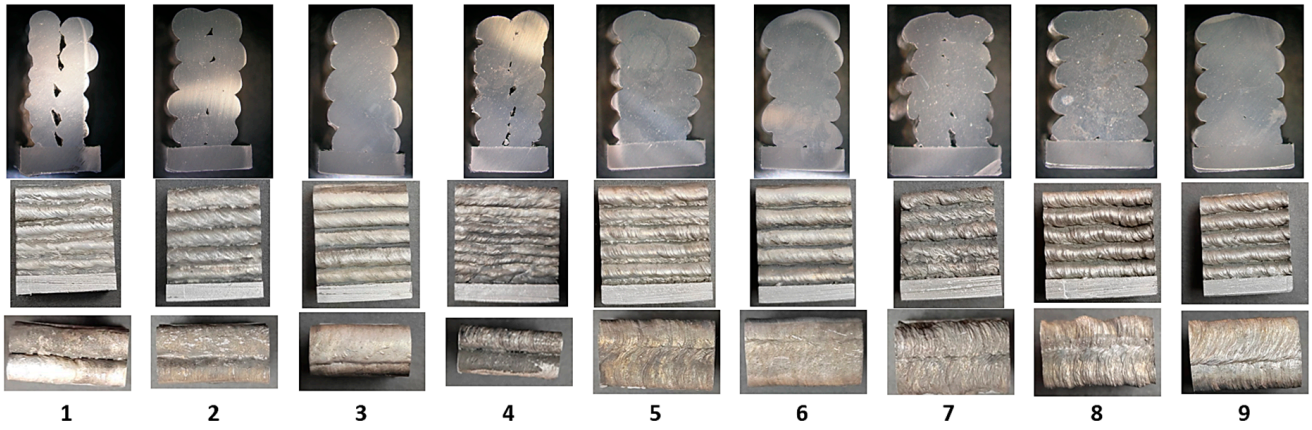


Figure 4. Macroscopic appearance of the nine WAAM walls produced according to the Taguchi L9 (3^3) experimental design.

Table 3 presents the output results obtained for the Taguchi analysis and optimization, including material utilization (*MU*), surface irregularity (*SI*), effective usable wall area (*EUWA*), lack-of-fusion (LoF) area within the *EUWA*, and surface roughness (*Sa*). It should be clearly stated that *EUWA* was experimentally determined from cross-sectional measurements of each specimen and was directly incorporated as a response variable in the regression modelling and Grey Relational Analysis, rather than being inferred from surface observations. Visual inspection reveals noticeable differences in wall geometry, surface morphology, and internal defect distribution among the specimens, indicating a strong influence of process parameter combinations on WAAM stability and wall quality. Although specimens 1 and 9 exhibit comparable material utilization values, their metallurgical bonding behaviour differs. Specimen 1 was produced with higher arc correction (40%) and lower current (40 A), which likely resulted in reduced penetration and less effective inter-pass remelting. In contrast, specimen 9 was fabricated with 0% arc correction and a higher current (60 A), which in the synergic regime corresponds to a higher wire feed rate and increased material deposition. The greater material supply combined with higher relative energy input promotes deeper penetration and more effective interlayer fusion, thereby reducing lack-of-fusion defects despite similar geometric efficiency indicators. Macrostructural comparison further indicates that lower current levels produced narrower beads and reduced melt pool dimensions, increasing susceptibility to lack-of-fusion defects, whereas higher current levels resulted in wider bead geometry and improved interpass remelting. Material utilization ranges from 70.7% to 81.2%, indicating differences in deposition efficiency and geometric stability of the walls. Surface irregularity values remain within a relatively narrow range (2.22–2.84 mm), while the *EUWA* shows more pronounced variation, with values between 160.2 mm^2 and 258.4 mm^2, highlighting the sensitivity of wall geometry to process conditions. The lack-of-fusion area within the *EUWA* varies significantly among experiments. While several specimens exhibit negligible LoF values (below 0.1%), others show markedly higher defect content, reaching up to 43.38%, which suggests unstable process conditions and insufficient fusion for certain parameter sets. It should be noted that the ImageJ-based defect quantification used for Table 3 was configured to capture only macroscopic lack-of-fusion (LoF) regions within the *EUWA*. The applied threshold parameters were selected to identify geometrically significant unfused regions, whereas fine, rounded gas pores were excluded from this specific LoF evaluation. Surface roughness (*Sa*) values range from 7.43 µm to 35.94 µm, further indicating differences in surface quality associated with the applied deposition parameters.

Table 3. Taguchi L9 (3^3) experimental plan output results.

Exp	Material Utilization *MU* (%)	Surface Irregularity *SI* (mm)	*EUWA* (mm^2)	Lack of Fusion Area in *EUWA* (%)	Surface Roughness *Sa* (µm)
1	81.2	2.22	182.4	43.38	34.17
2	74.5	2.48	172.6	9.07	19.02
3	76.2	2.47	214.1	0.02	17.77
4	72.5	2.34	160.2	16.33	30.48
5	79.9	2.29	190.0	0.03	14.09
6	74.8	2.52	215.7	0.08	7.43
7	77.4	2.34	162.8	2.94	35.94
8	70.7	2.84	204.0	0.1	31.39
9	80.5	2.29	258.4	0.02	27.09

After completing all experimental trials, the obtained dataset was employed to construct regression-based statistical models describing the relationship between the defined process parameters and the measured response variables. The models were derived strictly from experimentally acquired data and were applied to quantify the relative contribution of each process parameter to the system response [32]. Based on these regression formulations, response surface methodology (RSM) was subsequently adopted as an analytical framework to investigate parameter interactions and to provide a clear visual interpretation of their combined influence on the analyzed responses [33]. The complete set of regression equations corresponding to the three response variables is given in Equations (3)–(6).

$$\begin{aligned} MU = {} & 85.0 + 1.051\ Arc\ correction - 0.589\ Current - 1.81\ Gas\ flow \\ & -0.00514\ Arc\ correction{\cdot}Current - 0.0566\ Arc\ correction{\cdot}Gas\ flow \\ & +0.0654\ Current{\cdot}Gas\ flow \end{aligned} \quad (3)$$

$$\begin{aligned} SI = {} & 3.81 - 0.0621\ Arc\ correction - 0.0074\ Current - 0.037\ Gas\ flow \\ & +0.000657\ Arc\ correction{\cdot}Current + 0.00183\ Arc\ correction{\cdot}Gas\ flow \\ & -0.00057\ Current{\cdot}Gas\ flow \end{aligned} \quad (4)$$

$$\begin{aligned} EUWA = {} & 331.1 + 2.000\ Arc\ correction - 2.963\ Current - 21.34\ Gas\ flow \\ & -0.0140\ Arc\ correction{\cdot}Current - 0.1571\ Arc\ correction{\cdot}Gas\ flow \\ & +0.4717\ Current{\cdot}Gas\ flow \end{aligned} \quad (5)$$

$$\begin{aligned} Sa = {} & 296.1 - 2.198\ Arc\ correction - 6.81\ Current - 6.71\ Gas\ flow \\ & -0.338\ Gas\ flow{\cdot}Gas\ flow + 0.0638\ Arc\ correction{\cdot}Current \\ & -0.1085\ Arc\ correction{\cdot}Gas\ flow + 0.3513\ Current{\cdot}Gas\ flow \end{aligned} \quad (6)$$

Once the regression formulations for the WAAM process responses were defined, their agreement with the experimental dataset was examined. The predicted response values were compared with the experimentally recorded data obtained from the Taguchi L9 design. The goodness-of-fit was evaluated using the coefficient of determination (R^2) and the mean absolute percentage error (MAPE) as descriptive accuracy measures. The corresponding results are presented in Figure 5. Since the regression models were calibrated and assessed using the same experimental dataset, the reported statistical indicators reflect the fitting quality within the investigated design space rather than independent predictive validation. Therefore, the developed regression equations should be interpreted as calibrated empirical response functions describing parameter–response relationships within the selected experimental domain. On this basis, the models were subsequently employed in a response surface methodology (RSM) framework to explore interaction effects in an exploratory manner.

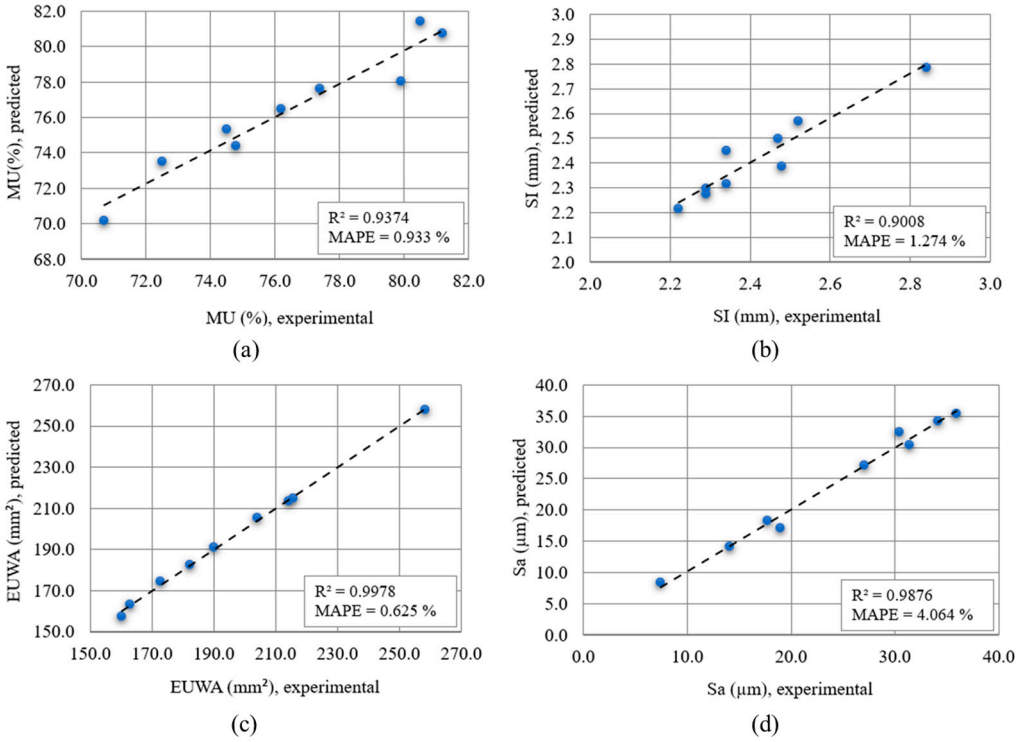


Figure 5. Agreement between experimental outcomes and regression model estimates for (**a**) material utilization, (**b**) surface irregularity, (**c**) *EUWA*, and (**d**) surface roughness.

Figures 6–9 present three-dimensional response surface visualizations illustrating the effect of selected WAAM process parameters on the primary output characteristics, including material utilization, surface irregularity, effective usable wall area, and surface roughness. Each surface plot evaluates the simultaneous variation in two process parameters, while the third parameter is fixed at its intermediate level. The response surface plots in Figure 6 for material utilization (*MU*) show that arc correction is the dominant parameter (for 60 A, especially), with a clear increase in *MU* as arc correction approaches zero, while current and gas flow modify this trend through secondary interaction effects. The higher current is associated with increased *MU*, which is attributed to increasing effective wall cross-section, whereas inappropriate gas flow levels reduce *MU* due to geometric instability of the deposited bead. The highest *MU* is obtained at zero arc correction combined with high current and a gas flow of 15 L/min, indicating that this parameter set maximizes the effective usable wall area while minimizing excess material formation. This confirms that arc stability is critical for converting increased deposition rate into usable wall geometry.

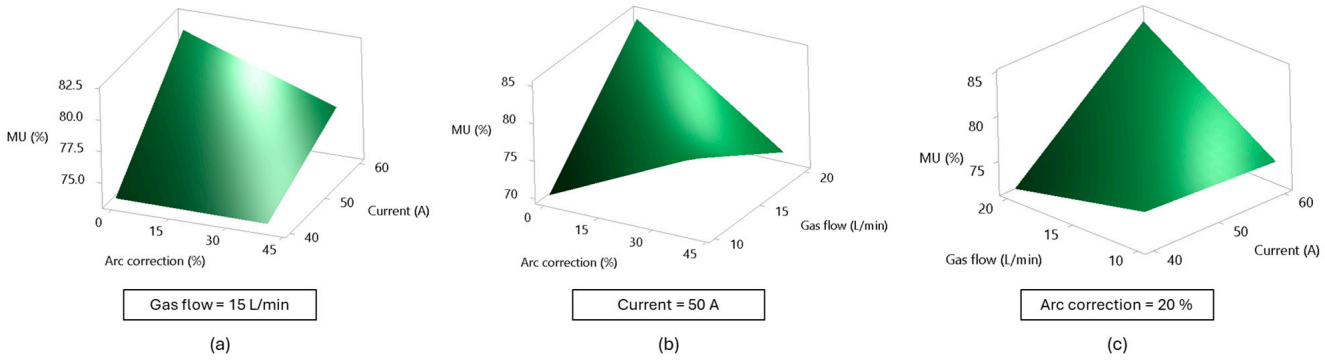


Figure 6. 3D response surfaces of material utilization as a function of interacting process parameters: (**a**) arc correction and current, (**b**) arc correction and gas flow, and (**c**) current and gas flow.

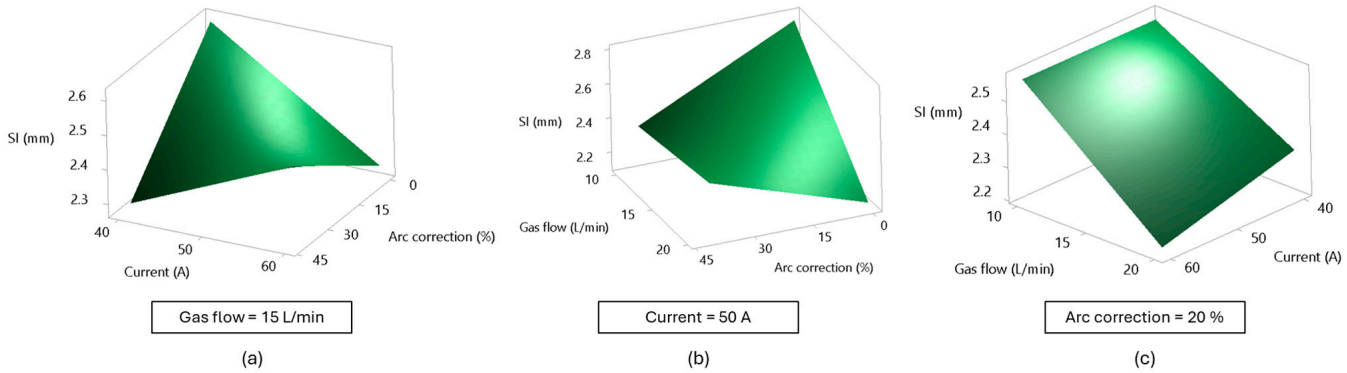


Figure 7. 3D response surfaces of surface irregularity as a function of interacting process parameters: (**a**) arc correction and current, (**b**) arc correction and gas flow, and (**c**) current and gas flow.

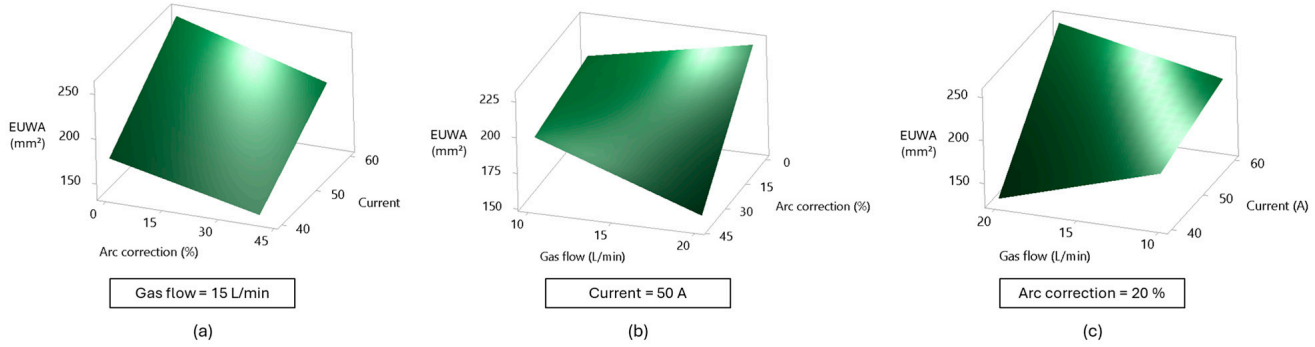


Figure 8. 3D response surfaces of *EUWA* as a function of interacting process parameters: (**a**) arc correction and current, (**b**) arc correction and gas flow, and (**c**) current and gas flow.

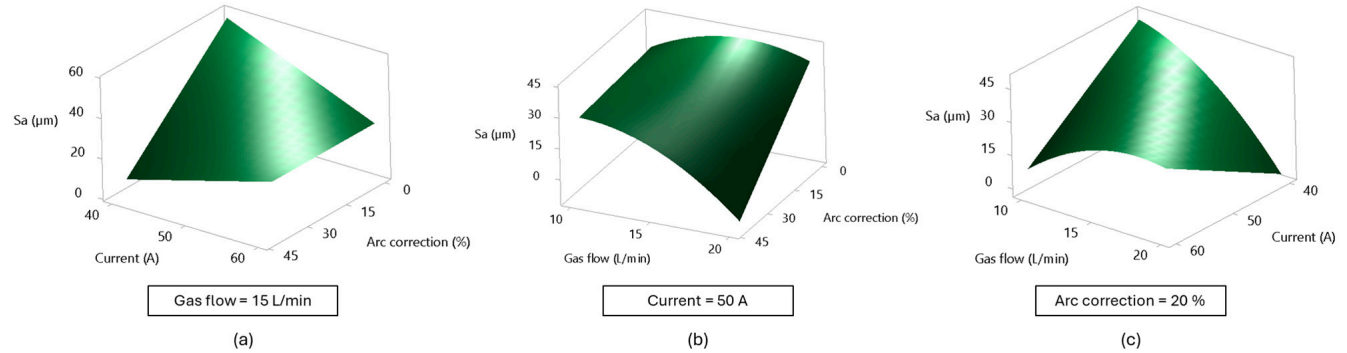


Figure 9. 3D response surfaces of surface roughness as a function of interacting process parameters: (**a**) arc correction and current, (**b**) arc correction and gas flow, and (**c**) current and gas flow.

The response surface plots in Figure 7 reveal a strong interaction between arc correction, current, and gas flow on surface irregularity (*SI*). Increasing current and gas flow intensify the heat input and molten pool dynamics, which promotes bead spreading and height fluctuations, whereas lower arc correction stabilizes the arc trajectory and leads to a more uniform material deposition. Surface irregularity is minimized under conditions of reduced arc correction combined with moderate current and shielding gas flow, indicating that SI is primarily governed by arc stability and controlled melt pool behaviour rather than by a single processing parameter alone. These trends indicate that surface irregularity is governed by melt pool stability rather than by heat input alone.

The response surface plots showed on Figure 8 for the effective usable wall area (*EUWA*) show that welding current has a dominant positive effect, as higher current is inherently associated with an increased wire feed rate and, consequently, a higher amount

of deposited material. However, the results clearly indicate that an increased deposition rate does not automatically translate into a larger usable wall area. Only under stable arc conditions—characterized by low arc correction and moderate shielding gas flow—does the additional deposited material effectively contribute to the growth of the wall cross-section. At higher arc correction levels or inappropriate gas flow rates, the excess material promotes bead spreading and geometric instability, reducing the effective load-bearing area. Therefore, maximum *EUWA* is achieved at high current combined with zero arc correction and a gas flow of 15 L/min, confirming that arc stability plays a critical role in converting increased material deposition into usable wall geometry. The results highlight that increased material deposition must be accompanied by stable arc conditions to effectively increase the load-bearing cross-section.

The response surface plots showed on Figure 9 for surface roughness (*Sa*) indicate that arc correction and welding current are the primary parameters governing surface quality in WAAM. Increasing arc correction leads to a pronounced increase in Sa due to enhanced arc wandering and irregular metal transfer, while higher current intensifies melt pool dynamics and promotes surface waviness when not adequately stabilized. Shielding gas flow exhibits a secondary but interactive effect, where insufficient or excessive flow levels adversely affect bead uniformity. The lowest *Sa* values are achieved at low arc correction combined with moderate current and a gas flow of 15 L/min, confirming that smooth surface formation is strongly linked to stable arc behaviour and controlled heat input rather than to increased material deposition alone. Surface roughness is therefore primarily linked to arc stability and controlled metal transfer.

At this point in the investigation, a multi-criteria optimization procedure was introduced with the objective of determining an optimal set of WAAM process parameters that ensures overall process performance. The optimization problem involved simultaneously addressing opposing requirements by reducing surface irregularity and surface roughness while enhancing material utilization and effective usable wall area. To accomplish this, a combined Taguchi–Grey Relational Analysis (GRA) framework was adopted. Within this framework, multiple response metrics are consolidated into a single Grey Relational Grade, enabling an integrated assessment of process behaviour and parameter effectiveness. A notable advantage of this technique lies in its operational efficiency, as it avoids intricate mathematical treatments and allows optimal parameter levels to be identified directly, without the need for additional computational steps [34]. The optimization workflow is initiated by determining signal-to-noise (S/N) ratios from the experimentally measured response data. The specific form of the S/N expression is selected according to the optimization goal assigned to each response variable. In this study, surface irregularity and surface roughness were defined as responses to be minimized, and their S/N ratios were evaluated using Equation (7). Conversely, material utilization and effective usable wall area were categorized as responses to be maximized, leading to the calculation of their corresponding S/N ratios based on Equation (8). Calculated S/N ratios are presented in Table 4.

$$S/N = -10\ \log_{10}\left(\frac{1}{n}\sum_{i=1}^{n} y_{ij}^2\right), \tag{7}$$

$$S/N = -10\ \log_{10}\left(\frac{1}{n}\right)\sum_{i=1}^{n} \frac{1}{y_{ij}^2}, \tag{8}$$

where n = number of replications, y_{ij} = observed response value, where $i = 1, 2, \ldots, n$; $j = 1, 2, \ldots, k$.

Table 4. S/N ratio responses.

Exp. No.	S/N Ratios			
	MU (%)	*SI* (mm)	*EUWA* (mm²)	*Sa* (μm)
1	38.191	−6.927	45.220	−30.673
2	37.443	−7.889	44.741	−25.584
3	37.639	−7.854	46.612	−24.994
4	37.207	−7.384	44.093	−29.680
5	38.051	−7.197	45.575	−22.978
6	37.478	−8.028	46.677	−17.420
7	37.775	−7.384	44.233	−31.112
8	36.988	−9.066	46.193	−29.936
9	38.116	−7.197	48.246	−28.656

Grey Relational Analysis (GRA) provides a structured methodology for evaluating multiple experimental responses by measuring their closeness to predefined ideal performance targets. This closeness is represented by the Grey Relational Coefficient (GRC), which quantifies the strength of correlation between a measured response and its ideal reference. A coefficient value equal to unity signifies perfect correspondence between the experimental and ideal responses. For multi-response optimization, the individual GRC values are aggregated into a single performance index known as the Grey Relational Grade (GRG). Within this analytical framework, the optimization objective is defined as the maximization of the GRG, regardless of whether the original response variables are associated with minimization or maximization criteria. As a result, the set of process parameters corresponding to the highest GRG is identified as the optimal solution in terms of overall process performance [35].

The application of Grey Relational Analysis (GRA) for multi-objective optimization follows a well-defined procedural framework. As a first step, the experimental response data are transformed onto a unified scale between 0 and 1, thereby limiting variability and enabling consistent comparison across different performance indicators. In this work, the normalization process was applied to the signal-to-noise (S/N) ratios corresponding to each response variable. The choice of normalization formulation was governed by the optimization goal assigned to each response. Specifically, responses designated for minimization, including surface irregularity and surface roughness, were normalized according to Equation (9), whereas responses intended for maximization—material utilization and effective usable wall area—were treated using the normalization expression given in Equation (10). The normalized response values obtained through this procedure are summarized in Table 5.

$$X_i^*(k) = \frac{\max X_i^0(k) - X_i^0(k)}{\max X_i^0(k) - \min X_i^0(k)}, \tag{9}$$

$$X_i^*(k) = \frac{X_i^0(k) - \min X_i^0(k)}{\max X_i^0(k) - \min X_i^0(k)}, \tag{10}$$

where $X_i^0(k)$ is the original sequence, $X_i^*(k)$ is the sequence after data pre-processing (normalization), $maxX_i^0(k)$ is the largest value in $X_i^0(k)$, and $minX_i^0(k)$ is the smallest value in $X_i^0(k)$.

In the subsequent phase of the Grey Relational Analysis procedure, Grey Relational Coefficients are evaluated for each response variable. The calculation of these coefficients follows the formulation provided in Equation (11).

$$\xi_i(k) = \frac{\Delta_{\min} + \zeta\Delta_{\max}}{\Delta_{0i}(k) + \zeta\Delta_{\max}}, \tag{11}$$

$\Delta_{0i}(k)$, Δmin, and Δmax are calculated using Equations (12)–(14).

$$\Delta_{0i}(k) = \|X_0^*(k) - X_i^*(k)\|, \tag{12}$$

$$\Delta_{\max} = \max\max\|X_0^*(k) - X_i^*(k)\|, \tag{13}$$

$$\Delta_{\min} = \min\min\|X_0^*(k) - X_i^*(k)\|, \tag{14}$$

where ζ is the distinguishing coefficient in the range of [0,1] (in general, $\zeta = 0.5$), $\Delta_{0i}(k)$ is the deviation sequence for the reference sequence, $X_0^*(k)$ is the reference sequence ($X_0^*(k) = 1$, where $k = 1, 2 \ldots n$, n is the number of responses), and $X_i^*(k)$ is the specific comparison sequence.

Table 5. Normalization results.

Exp. No.	Normalization			
	***MU* (%)**	***SI* (mm)**	***EUWA* (mm²)**	***Sa* (μm)**
1	1.000	0.000	0.271	0.968
2	0.378	0.450	0.156	0.596
3	0.541	0.433	0.607	0.553
4	0.182	0.214	0.000	0.895
5	0.883	0.126	0.357	0.406
6	0.407	0.515	0.622	0.000
7	0.654	0.214	0.034	1.000
8	0.000	1.000	0.506	0.914
9	0.937	0.126	1.000	0.821

The concluding step of the Grey Relational Analysis procedure consists of evaluating the Grey Relational Grade (GRG) in accordance with Equation (15), under the assumption of equal weighting assigned to all response variables, thereby ensuring a neutral multi-objective evaluation without introducing subjective prioritization of any specific performance indicator. Based on this calculation, the Grey Relational Coefficients (GRCs), the derived GRG values, and the corresponding ranking of the experimental runs were obtained, where higher rankings indicate larger GRG values and lower rankings reflect poorer overall performance. A summary of these results is provided in Table 6.

$$GRG = \frac{1}{n}\sum_{k=1}^{n} \xi_i(k), \tag{15}$$

Table 6. Overview of Grey Relational Coefficients (GRCs), aggregated Grey Relational Grade (GRG), and corresponding performance rankings.

Exp. No.	GRCs				GRG	Rank
	***MU* (%)**	***SI* (mm)**	***EUWA* (mm²)**	***Sa* (μm)**		
1	1.000	0.333	0.407	0.940	0.670	3
2	0.446	0.476	0.372	0.553	0.462	9
3	0.521	0.469	0.560	0.528	0.519	5
4	0.379	0.389	0.333	0.827	0.482	7
5	0.811	0.364	0.437	0.457	0.517	6
6	0.458	0.507	0.570	0.333	0.467	8
7	0.591	0.389	0.341	1.000	0.580	4
8	0.333	1.000	0.503	0.853	0.672	2
9	0.889	0.364	1.000	0.736	0.747	1

To examine the effect of the selected process parameters on the Grey Relational Grade (GRG) and to evaluate their relative influence, a main effects diagram for GRG was constructed, as presented in Figure 10. The gradients of the plotted trends indicate that each of the three analyzed parameters exerts a discernible impact on the GRG response. In addition, the main effects plot allows an initial estimation of the parameter levels associated with the highest average GRG values, which are indicative of improved overall process performance. Based on this preliminary assessment, the maximum GRG was first observed at an arc correction of 0%, a current of 60 A, and a gas flow rate of 10 L/min, which is consistent with the response values summarized in Table 7. Furthermore, Table 7 offers a quantitative comparison of parameter importance by evaluating the difference between the maximum and minimum mean GRG values. This range-based analysis indicates that arc correction is the dominant factor influencing GRG, followed by gas flow, whereas current shows the weakest effect among the considered parameters. Nevertheless, a more precise determination of the optimal parameter combination requires the consideration of interaction effects on the GRG response. These interactions are depicted in Figure 11. A closer inspection of the interaction plots—particularly the green and blue trend lines—reveals that the initially identified parameter settings should be adjusted. As a result, the final optimal process conditions were established as an arc correction of 0%, a current of 60 A, and a gas flow of 15 L/min.

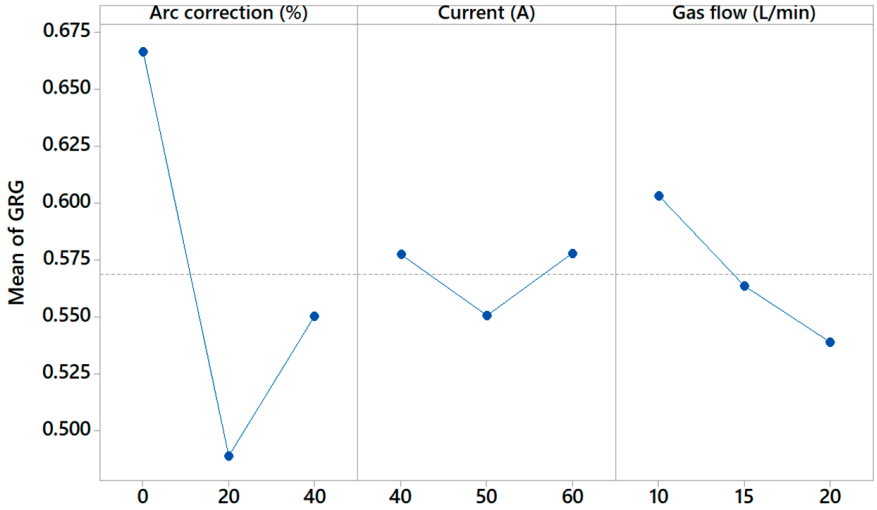


Figure 10. Main effects plots illustrating the influence of individual process parameters on the Grey Relational Grade (GRG).

Table 7. Response values of the Grey Relational Grade (GRG) across different process parameter levels.

Process Parameters	Operating Levels			Max-Min	Rank
	1	2	3		
Arc correction	0.6666	0.4888	0.5504	0.1778	1
Current	0.5774	0.5505	0.5779	0.0274	3
Gas flow	0.6031	0.5637	0.5390	0.0641	2

To achieve a more comprehensive understanding of how interactions among process parameters affect the Grey Relational Grade (GRG) and to identify favourable operating domains for the WAAM process, a regression-based mathematical formulation of the GRG response was established. The resulting regression expression is given in Equation (16). Model reliability was examined by comparing the GRG values calculated from experimental data, as listed in Table 6, with those estimated by the regression model. The

outcomes of this comparison, along with the associated validation indicators (R^2 = 0.957 and MAPE = 3.113%), are illustrated in Figure 12, confirming strong agreement between predicted and calculated values and verifying the suitability of the model for interaction analysis. In addition, Figure 12 delineates a set of Pareto-optimal solutions, corresponding to parameter combinations for which further improvement of one objective would necessarily lead to the deterioration of at least one other objective. In multi-objective optimization, the Pareto front represents a set of non-dominated solutions that define the optimal trade-off boundary between competing performance criteria, rather than a single absolute optimum. In this study, the competing objectives involve reducing surface irregularity (*SI*) and surface roughness (*Sa*) while simultaneously increasing material utilization (*MU*) and effective usable wall area (*EUWA*). The resulting Pareto front thus defines a balanced compromise region between surface irregularity and material efficiency. Although the ninth experimental run exhibits the highest Grey Relational Grade and is identified as the overall optimal configuration, additional Pareto-optimal solutions are also observed, notably experimental runs 1 and 8, which represent alternative trade-off combinations between geometric stability and surface quality. This confirms that the optimization problem cannot be interpreted solely on the basis of a single response metric or direct comparison of raw experimental data. Among the identified Pareto-optimal configurations, the highest predicted GRG is associated with the ninth experimental run, characterized by an arc correction of 0%, a current of 60 A, and a gas flow rate of 15 L/min. This finding is fully aligned with the interaction behaviour previously observed in Figure 11.

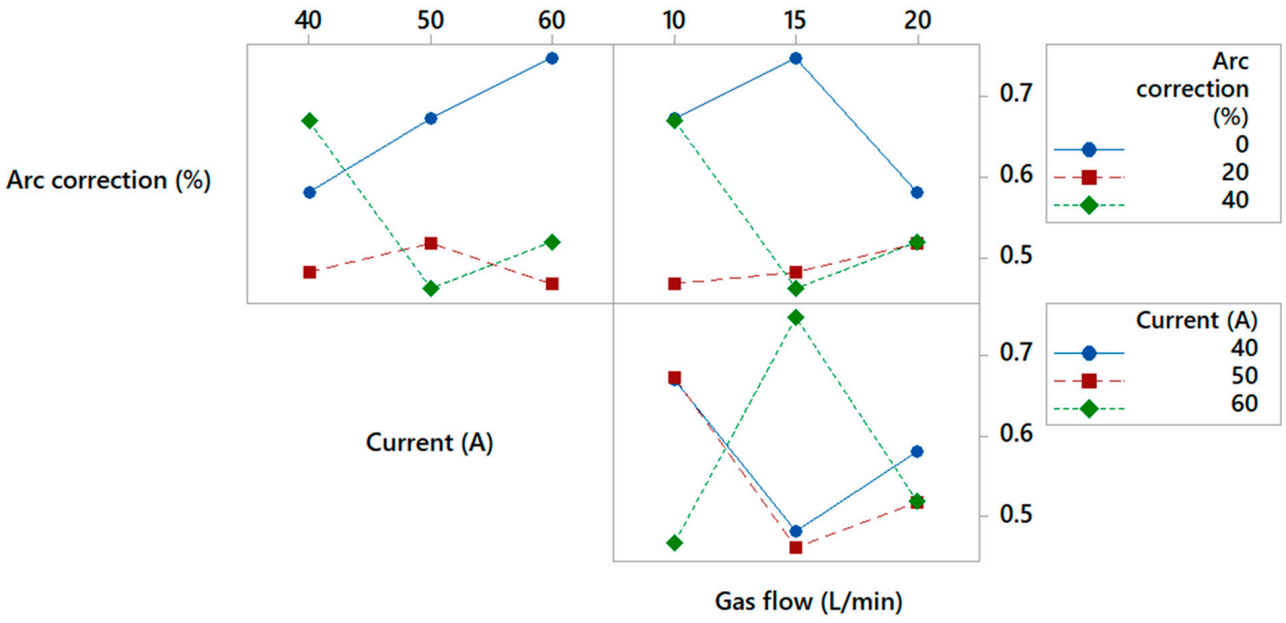


Figure 11. Influence of interacting process parameters on GRG depicted by interaction effects plots.

$$GRG = 3.074 + 0.00216\ Arc\ correction - 0.0508\ Current - 0.1665\ Gas\ flow + 0.000124\ Arc\ correction{\cdot}Current - 0.001050\ Arc\ correction{\cdot}Gas\ flow + 0.003572\ Current{\cdot}Gas\ flow \quad (16)$$

To provide a clearer representation of the Pareto front and to delineate favourable operating windows, three-dimensional response surface visualization accompanied by a contour plot was constructed, as shown in Figure 13. These graphical representations examine the combined variation in arc correction and current while maintaining the gas flow at a constant value. In support of this analysis, an analysis of variance (ANOVA)

was conducted at a 95% confidence level, with the corresponding results summarized in Table 8. The ANOVA results indicate that arc correction contributes the largest proportion of variance to the Grey Relational Grade (GRG), followed by shielding gas flow, while welding current shows the smallest contribution. However, due to the limited number of experimental runs, none of the investigated parameters reached statistical significance at the 95% confidence level. The dark green regions visible in the contour map of Figure 13 mark the optimal WAAM processing domains, where the fabricated components exhibit the most favourable balance between surface quality and material utilization.

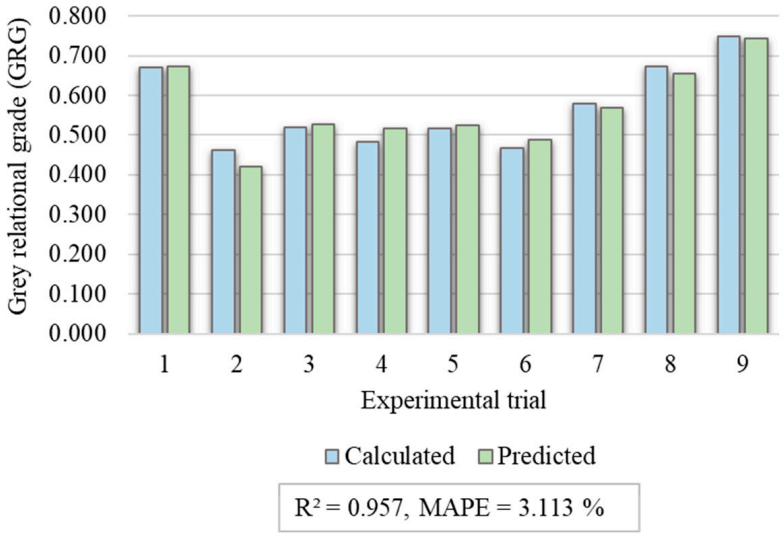


Figure 12. Comparison between computed and regression-estimated Grey Relational Grade (GRG) values.

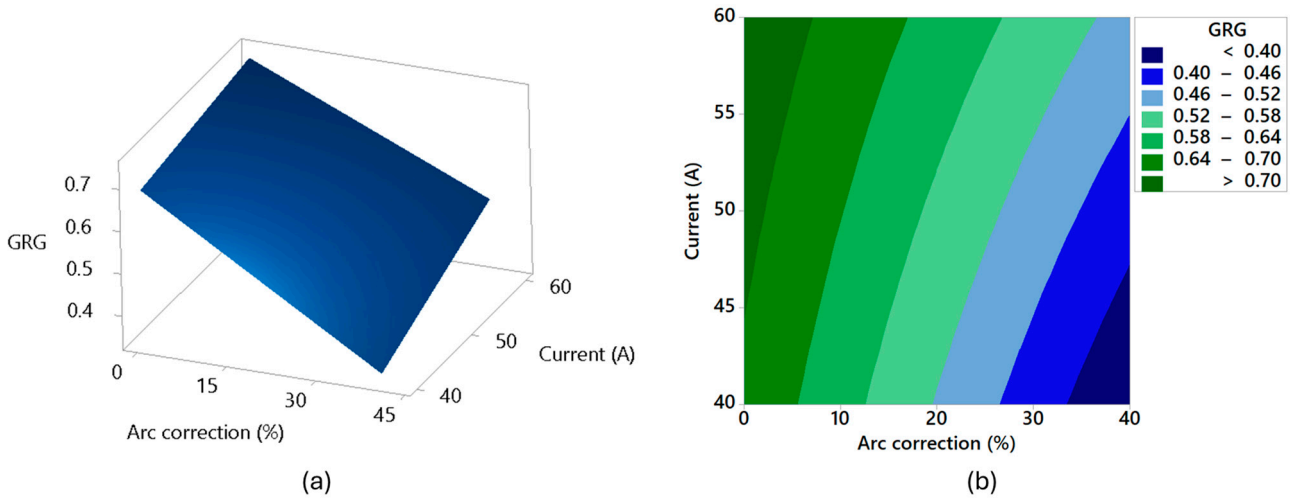


Figure 13. Effect of coupled arc correction and current on GRG under a constant gas flow of 15 L/min, shown as (**a**) a 3D response surface and (**b**) a contour map.

Table 8. ANOVA-based evaluation of the Grey Relational Grade (GRG) response.

Source	DF	SS	MS	F-Value	*p*-Value	Contribution (%)
Arc correction	2	0.048900	0.024450	1.59	0.386	55.97
Current	2	0.001476	0.000738	0.05	0.954	1.68
Gas flow	2	0.006281	0.003140	0.20	0.830	7.18
Error	2	0.030705	0.015353			
Total	8	0.087362				

It should be noted that, due to the limited number of experimental runs in the Taguchi L9 design, the statistical power of factor significance testing is inherently constrained. Therefore, the observed parameter effects should be interpreted primarily as indicative trends within the investigated experimental domain rather than as statistically conclusive evidence of significant factor influence.

To assess the effectiveness of the identified optimal WAAM process parameter configuration, a comparative evaluation was carried out between the Grey Relational Grade (GRG) values obtained for the initial parameter settings and those corresponding to the optimized conditions, as summarized in Table 9. The results demonstrate an improvement of approximately 55% in the GRG value, reflecting a marked enhancement in the overall performance of the WAAM process. This significant increase confirms the capability of the Grey Relational Analysis (GRA)-based optimization approach to simultaneously address multiple, often competing, performance objectives. By integrating surface irregularity–related responses with material efficiency indicators into a single performance index, the GRA framework enables a balanced and systematic optimization of process parameters. Consequently, the applied optimization strategy not only improves individual response characteristics but also leads to a substantial overall process improvement, highlighting the practical relevance and robustness of the GRA methodology for multi-objective optimization of complex additive manufacturing processes.

Table 9. Optimized process parameter settings and corresponding improvement in Grey Relational Grade.

Process Parameters Settings	Representative Non-Optimal Parameter Set	Optimal Conditions
Arc correction (%)	20	0
Current (A)	40	60
Gas flow (L/min)	15	15
MU (%)	72.5	80.5
SI (mm)	2.34	2.29
EUWA (mm^2)	160.2	258.4
Sa (μm)	30.48	27.09
GRG	0.482	0.747
Improvement (%)	-	54.9

3.2. Mechanical Properties

After Taguchi-based optimization, the optimized parameter set (Exp. 9, Table 1) was used to fabricate the wall used for mechanical testing. Figure 14 shows the microhardness measurement HV1. The measured hardness values ranged approximately between 72 and 85 HV. The measured hardness values are slightly lower than those typically reported for wrought EN AW 5356 (approximately 75–85 HV), which is consistent with the cast-like solidification structure inherent to WAAM processing. However, the obtained values fall within the range commonly reported for WAAM-fabricated Al–Mg alloys (approximately 64–76 HV) in previous studies [36,37], confirming the structural adequacy of the deposited material. Overall, the hardness distribution along the build height was relatively uniform, with moderate local variations. Slightly higher hardness values were observed in the mid-to-upper regions of the wall, which can be attributed to thermal cycling effects inherent to the WAAM process, such as repeated reheating and cooling during layer-by-layer deposition. The absence of a pronounced hardness gradient indicates stable deposition conditions and relatively consistent material response throughout the build height. Although a linear trend line suggests a slight decrease in hardness with increasing height, the low coefficient of determination (R^2 = 0.0542) confirms that local microstructural heterogeneity and layer-

dependent thermal effects dominate over any global monotonic trend. This result can be further explained by the fact that the investigated aluminum Al-5356 is a non-heat-treatable alloy [36].

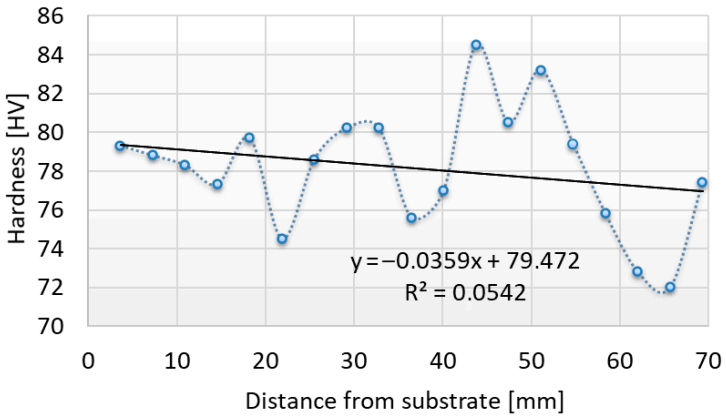


Figure 14. Hardness measurement from the bottom to the top of the specimen.

The tensile stress–strain curves of all three WAAM specimens exhibit characteristic ductile behaviour without a clearly defined yield point, which is typical for aluminum alloys processed by wire arc additive manufacturing. Due to the absence of a clearly defined yield plateau, which is typical for WAAM-fabricated aluminum alloys, yield strength was not explicitly reported. Such continuous yielding behaviour has been reported for WAAM-fabricated aluminum alloys and is typically associated with microstructural heterogeneity, layered solidification structures, and the absence of Lüders-type deformation phenomena [10,11]. Furthermore, strain measurement was derived from machine crosshead displacement rather than extensometer-based acquisition, limiting the reliable determination of elastic modulus. Therefore, ultimate tensile strength and elongation were considered the most representative mechanical indicators under the applied testing conditions. The ultimate tensile strength ranges from 152 MPa to 208 MPa, indicating a pronounced scatter in mechanical response; see Table 10. Such variability in both strength and elongation reflects local microstructural heterogeneity and spatial defect distribution within the multi-pass WAAM structure. The results for tensile strength obtained from vertically extracted specimens are in good agreement with some previously reported data for the same filler material [10]; however can be improved to get closer to standard as reported in some previous studies for single wall WAAM researches [36–38]. It should be noted that tensile testing was performed on three specimens extracted from the optimized wall configuration. The observed standard deviation reflects local microstructural heterogeneity and spatial defect distribution inherent to multi-pass WAAM structures. While this sample size limits statistical robustness, the mechanical testing was intended to validate the optimized parameter set rather than to serve as a primary optimization variable. Future work will include expanded mechanical sampling to improve statistical confidence, but also changing parameters to improve mechanical properties.

The average elongation at fracture of 9.6% indicates moderate ductility of the WAAM-fabricated AlMg5 material. Although lower than that of wrought EN AW 5356, this value remains acceptable for structural WAAM applications, considering the intrinsic anisotropy and residual porosity typical of additively manufactured components. Due to the limited number of specimens, a direct quantitative correlation between specific defect characteristics and mechanical response cannot be conclusively established within the scope of this study. These findings suggest that optimization should extend beyond single-wall geomet-

ric criteria and must account for deposition strategies in thicker multi-bead walls, where internal bonding and defect accumulation critically influence mechanical performance.

Table 10. Tensile test results for the deposited WAAM wall.

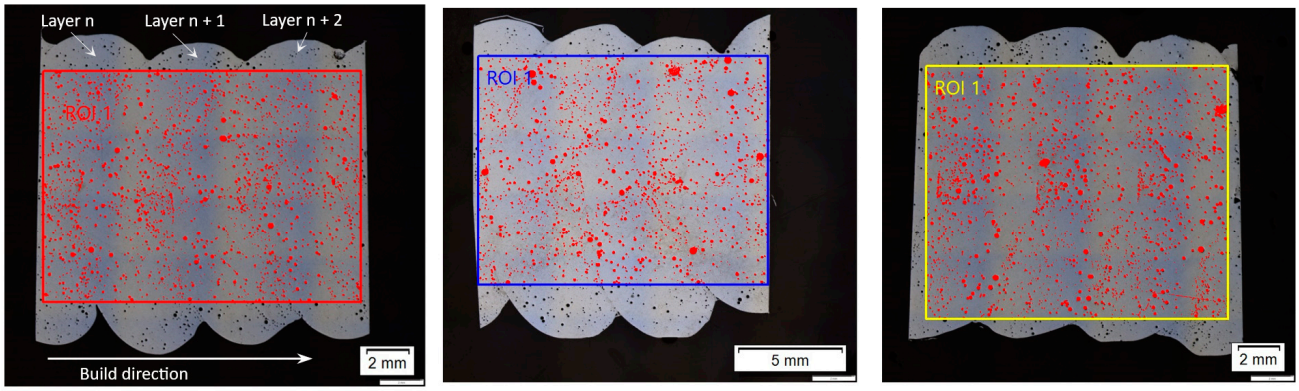
Specimen	Tensile Strength (MPa)	Engineering Strain (%)
1	152 MPa	9.3%
2	164 MPa	9.0%
3	208 MPa	10.6%
Average	175 MPa	9.63%
Standard deviation	29 MPa	0.83%
Reference AWS 5356 [39]	270 MPa	17%

3.3. Metallography

3.3.1. Optical Microscopy and Porosity Analysis

An Olympus optical microscope was employed to analyze the microstructural appearance of the WAAM-deposited wall from the bottom to the top. Both porosity and grain morphology were examined at three locations along the build height. The first specimen segment was extracted starting at 5 mm above the substrate, with a section height of 15 mm. The second segment was taken at 30 mm from the substrate, and the third at 55 mm from the substrate. Figure 15 shows the porosity distribution within the wall area at three different heights from the substrate. The analyzed regions of interest (ROIs) are highlighted, with pores identified and quantified using image analysis. The results indicate a gradual increase in porosity with increasing build height, from 3.20% at 5 mm to 3.39% at 30 mm and 3.49% at 55 mm. The measured porosity levels (3.20–3.49%) fall within the typical range reported for WAAM aluminum alloys, indicating a reasonably stable deposition process. Hauser et al. reported that, in CMT-based WAAM of AlSi5 filler metal, porosity was dominated by process-related macropores with sizes ranging from approximately 0.5 mm up to 2 mm, and further showed that excessive shielding gas flow promotes convective cooling of the melt pool, limiting pore escape and leading to increased retained porosity [40]. Arana et al. reported that for the 20-layer WAAM walls made from filler all AlMg5, the porosity ranged from approximately 3.7% under insufficient shielding conditions to below 0.06% when optimized shielding gas flow and deposition strategy were applied, demonstrating that porosity in multilayer WAAM is highly sensitive to process stability rather than to material deposition alone. Even a porosity level as high as 2.86% exhibited a limited effect on mechanical properties when pores were randomly distributed and not clustered or concentrated within the interlayer regions [41]. Wieczorowski et al. demonstrated that the CMT-based WAAM of AA5356 produces walls with very low porosity levels (<0.12 vol.%), as quantified by micro-computed tomography, and that increasing travel speed and cooling time reduces pore size and total pore volume by lowering heat accumulation. Importantly, no direct correlation was found between porosity and tensile properties, indicating that at such low and non-clustered porosity levels, the mechanical performance of WAAM Al–Mg walls is not significantly affected [38]. The observed porosity in this work is primarily attributed to hydrogen entrapment and local solidification dynamics typical of aluminum WAAM processes. Within the investigated gas flow range (10–20 L/min), no systematic correlation between shielding gas level and porosity content was identified, suggesting that arc stability and thermal conditions played a more dominant role. Lack-of-fusion defects are considered to originate mainly from insufficient inter-pass remelting, material deposition, and localized arc instability rather than from shielding deficiencies. Furthermore, in this work, it is observed that the slight

increase in porosity toward the top of the wall is consistent with thermal accumulation effects commonly observed in WAAM structures. The presence of porosity at all investigated heights indicates that defect formation is not limited to a specific region of the wall, but occurs throughout the build with a layer-dependent and spatially non-uniform distribution governed by local process conditions and the applied deposition strategy. This behaviour contributes to the observed scatter in tensile mechanical properties. These findings can also help explain the scatter in mechanical properties obtained from tensile testing.



(a) 5 mm from substrate (3.20 % porosity)

(b) 30 mm from substrate (3.39 % porosity)

(c) 55 mm from substrate (3.49 % porosity)

Figure 15. Porosity distribution along the height of the WAAM wall at (**a**) 5 mm, (**b**) 30 mm, and (**c**) 55 mm from the substrate. Regions of interest (ROIs) used for image analysis are indicated, and the corresponding porosity values are reported for each location.

Figure 16 shows the optical micrographs and macrostructure of WAAM specimen 3 at different magnifications. Figure 16a presents the macro cross-section of the deposited wall, revealing a relatively uniform bead geometry with visible internal porosity distributed throughout the section, but also visible interlayers during wall deposition, defects, and crystal grains. Figure 16b–d show optical micrographs at increasing magnifications, highlighting the grain morphology, pore distribution, and defects within the deposited material. The microstructure consists of predominantly equiaxed grains with local variations in grain size, indicating the influence of repeated thermal cycling during layer-by-layer deposition. Smaller grains are observed at the new layers' starting point, while coarser grains are visible in the middle part of the interlayers of the aluminum WAAM walls. The visible interlayer boundaries confirm the layered nature of the WAAM process and the influence of repeated thermal cycles on microstructural evolution. In addition, occasional elongated defects (porosity, lack of fusion areas, and segregations) aligned with the deposition direction can be identified, which may be associated with interlayer boundaries or local lack-of-fusion regions. However, the relatively homogeneous distribution of gas porosity throughout the observed regions confirms that defect formation is not localized but occurs across the entire wall thickness. These observations are consistent with the porosity quantification results and help explain the mechanical performance and results scatter obtained for the WAAM specimen, particularly the balance between tensile strength and ductility.

Figure 17 presents a set of optical micrographs at different magnifications illustrating the microstructural characteristics of the WAAM-deposited AlMg5 wall to confirm some of the conclusions from Figure 16. A panoramic view reveals the layered nature of the deposited structure, with clearly distinguishable interlayer boundaries extending across the wall height. At higher magnifications, distinct interlayer regions are observed, frequently accompanied by isolated pores and localized defect clusters preferentially located along these boundaries. These defects mainly appear as rounded or irregular pores and isolated dark

regions, indicating that defect formation and stabilization are influenced by local remelting phenomena and repeated thermal cycling associated with successive layer deposition. Importantly, no continuous or propagating cracks were observed across the investigated regions, as may be inferred from the lower-magnification images in Figure 16. Although certain features may initially resemble crack-like defects in lower-magnification images, higher-magnification observations confirm that these features correspond to clusters of pores or locally altered microstructural regions rather than classical solidification or thermal cracking. Local contrast variations and dark regions within the matrix are also visible, particularly near interlayer boundaries. These features are attributed to differences in grain morphology, etching response, and the presence of locally distinct microstructural constituents, rather than pronounced chemical segregation. Although interpass cooling to room temperature was applied after each double layer, the observed microstructural features indicate that differences in thermal boundary conditions and repeated localized reheating continue to play a significant role in defect formation and microstructural evolution.

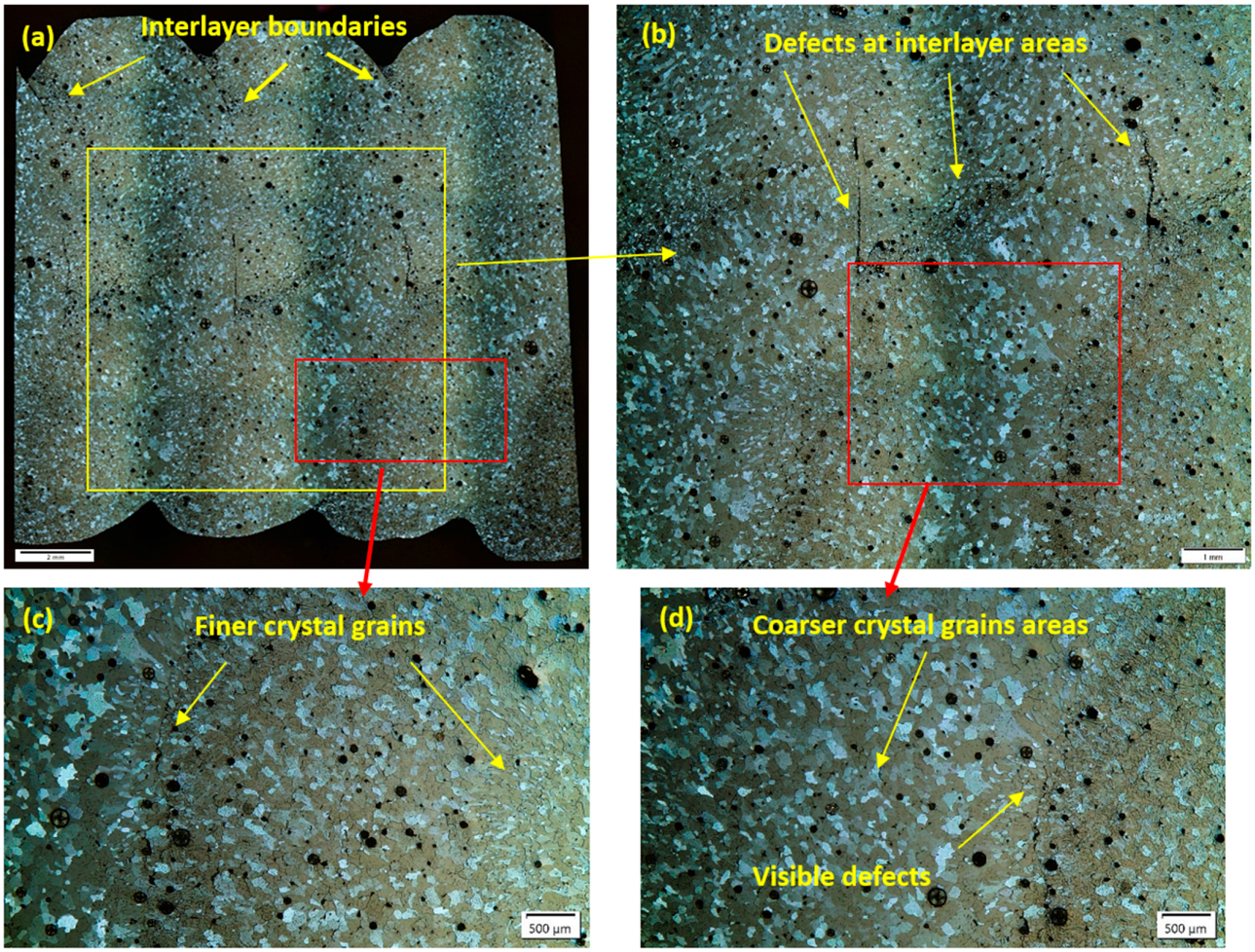


Figure 16. Optical microscopy images of WAAM specimen 3 showing (**a**) overall panorama view with clearly visible interlayer boundaries and crystal grains, (**b**) magnified view of an interlayer region highlighting localized defect accumulation, (**c**) area with finer crystal grains, and (**d**) region characterized by coarser crystal grains with visible defects.

Figure 18 shows the optical microstructures of the WAAM-deposited AlMg5 wall at selected locations within the coarser-grained regions located in the middle of the interlayers. Close to the substrate (5 mm), finer and more irregular grain morphologies are observed, which can be attributed to higher cooling rates and efficient heat extraction

through the substrate. At mid-height (30 mm), grains appear more equiaxed and coarser. This microstructural evolution is associated with reduced effective cooling rates and the cumulative influence of repeated local reheating caused by successive layer deposition, despite controlled cooling to room temperature after each double layer. Toward the upper region of the wall (55 mm), further grain coarsening and increased heterogeneity in grain size are evident. This behaviour reflects differences in thermal boundary conditions and lower thermal gradients due to the increasing distance from the substrate, rather than continuous heat accumulation. Although interpass cooling to room temperature was applied, the thermal history of the deposited material remains height-dependent due to changes in heat dissipation pathways and repeated localized reheating effects. Since no quantitative grain size measurements were performed, the interpretation remains qualitative.

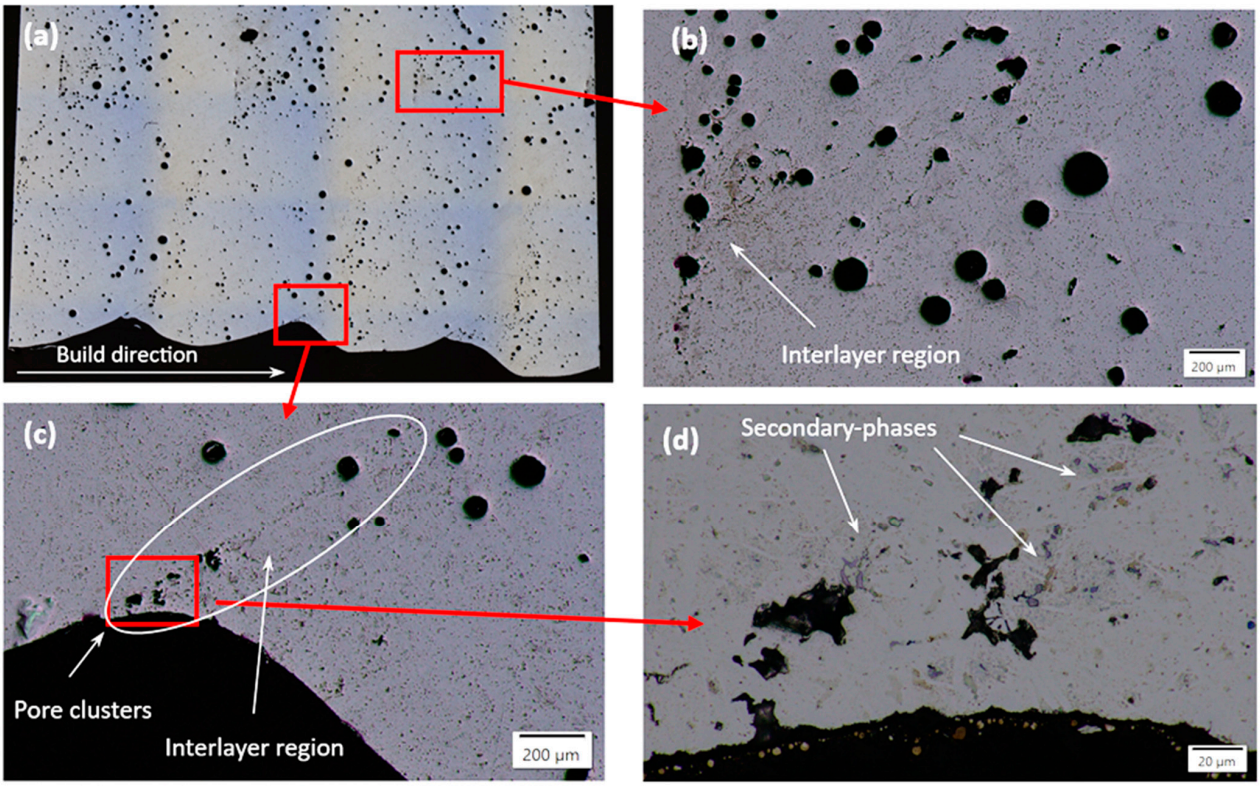


Figure 17. Optical micrographs of the WAAM-deposited AlMg5 wall at different magnifications showing the (**a**) panoramic view of the layered structure, (**b**) interlayer region with localized porosity and defects, (**c**) view of pore clusters and defect-rich areas near the interlayer boundary, and (**d**) high-magnification image of localized microstructural heterogeneity and secondary-phase-rich regions.

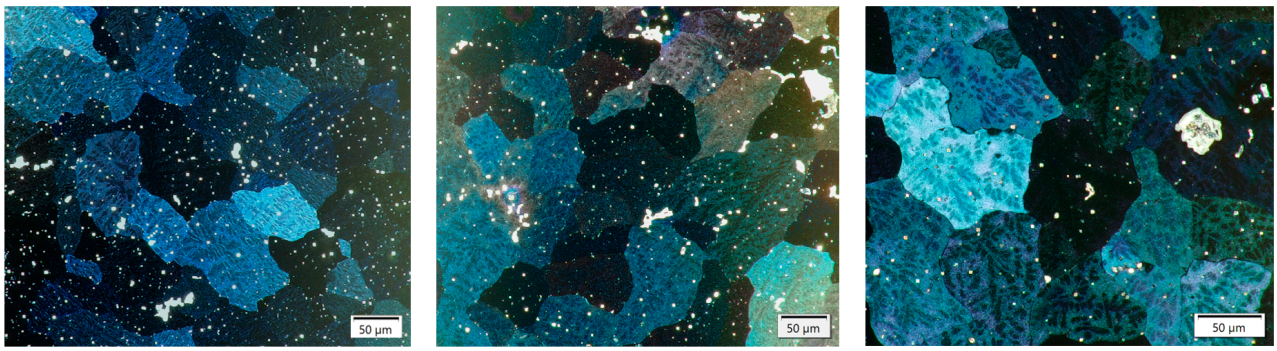


Figure 18. Microstructural evolution along the height of the WAAM walls at (**a**) 5 mm, (**b**) 30 mm, and (**c**) 55 mm from the substrate.

3.3.2. Scanning Electron Microscopy

Figure 19 shows SEM micrographs and corresponding EDS elemental maps of the WAAM-deposited AlMg5 specimen, highlighting the microstructural features and elemental distribution within the analyzed area. SEM and EDS analyses revealed a predominantly homogeneous aluminum matrix with magnesium uniformly distributed throughout the microstructure. Localized iron-rich particles were identified, corresponding to bright features in the SEM images, indicating the presence of Fe-based intermetallic phases (e.g., Al–Fe or Al–Fe–Si compounds). Silicon and manganese were detected in minor amounts and appeared either finely dispersed or associated with isolated secondary particles. Porosity was observed as discrete voids without elemental enrichment, suggesting a process-related origin rather than chemical segregation. Overall, no significant elemental segregation or continuous secondary phase formation was detected. No evidence of continuous solidification or hot cracking was observed, and SEM–EDS analysis did not indicate pronounced elemental segregation that could promote such defects. A more detailed analysis is beyond the scope of the present study, as its inclusion would significantly increase the length and complexity of the work, and will therefore be addressed in future research.

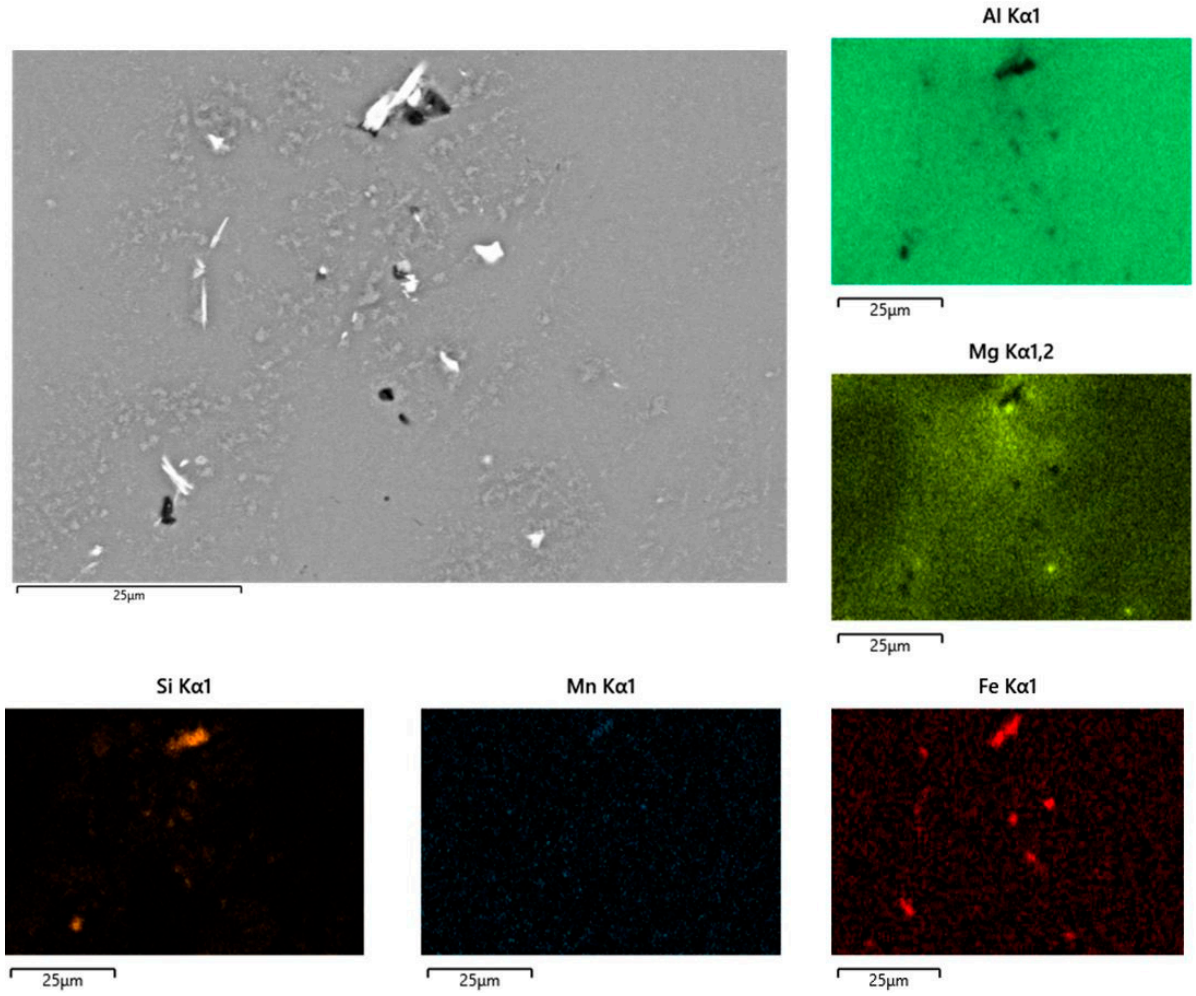


Figure 19. SEM micrographs and corresponding EDS elemental maps of the WAAM-deposited AlMg5 specimen.

4. Conclusions

The conducted research confirmed that the quality of double-pass WAAM walls cannot be adequately described by geometric characteristics alone. Instead, the structural

integrity and mechanical response appear to be influenced by interlayer microstructural heterogeneity and spatially non-uniform defect distribution inherent to the multi-pass deposition strategy.

The main findings can be summarized as follows:

- The Taguchi L9 (3^3)–GRA approach successfully identified arc correction as the dominant parameter governing double-wall GMAW-based WAAM performance, confirming that arc stability primarily controls material utilization, geometric accuracy, and surface quality.
- GRG analysis showed that arc correction had the strongest influence, followed by shielding gas flow, while welding current had the lowest effect within the investigated range. The optimal parameter set (0% arc correction, 60 A, 15 L/min) achieved the highest GRG and represents a balanced trade-off between geometric efficiency and process stability.
- Pronounced grain heterogeneity was observed along the build height. Finer grains formed near interlayer boundaries due to repeated thermal cycling and partial remelting, while coarser grains developed within individual layer cores.
- Porosity (3.2–3.5%) and lack-of-fusion defects were spatially concentrated in interlayer and double-pass overlap regions, confirming location-dependent defect formation.
- Hardness ranged between 72 and 85 HV along the build height, showing local fluctuations associated with microstructural heterogeneity and repeated thermal cycling. The WAAM-fabricated AlMg5 walls exhibited an average UTS of 175 MPa and 9.6% elongation. The observed mechanical scatter is consistent with the spatial distribution of porosity (3.2–3.5%) and localized lack-of-fusion defects concentrated near interlayer regions, indicating that inter-pass remelting and grain morphology evolution critically influence mechanical performance in multi-pass WAAM structures.
- These results indicate that while geometric indicators are effective for comparative process optimization, they are not sufficient for comprehensive structural qualification. For multi-pass WAAM structures, geometric evaluation should therefore be complemented by metallographic and mechanical characterization.

Author Contributions: Conceptualization, J.K.; methodology, J.K., A.N. and I.P.; software, J.K., A.N. and I.P.; validation, J.K., A.N. and I.P.; formal analysis, J.K., I.D.L. and I.P.; investigation, J.K. and A.N.; resources, J.K.; data curation, J.K. and I.P.; writing—original draft preparation, J.K., I.P. and I.D.L.; writing—review and editing, J.K., A.N., I.P. and I.D.L.; visualization, J.K. and I.P.; supervision, J.K.; project administration, J.K.; funding acquisition, J.K. All authors have read and agreed to the published version of the manuscript.

Funding: This work was supported by the European Union under the NextGenerationEU instrument, through the Recovery and Resilience Mechanism, within the institutional research project AIMTECH 4.5 (IP-UNIST-07), implemented by the Ministry of Science, Education and Youth of the Republic of Croatia.

Institutional Review Board Statement: Not applicable.

Informed Consent Statement: Not applicable.

Data Availability Statement: The data presented in this study are available on request from the corresponding author.

Conflicts of Interest: The authors declare no conflicts of interest.

References

1. Ding, D.; Pan, Z.; Cuiuri, D.; Li, H. Wire-feed additive manufacturing of metal components: Technologies, developments and future interests. *Int. J. Adv. Manuf. Technol.* **2015**, *81*, 465–481. [CrossRef]

2. Feng, Y.; Fan, D. Investigating the Forming Characteristics of 316 Stainless Steel Fabricated through Cold Metal Transfer (CMT) Wire and Arc Additive Manufacturing. *Materials* **2024**, *17*, 2184. [CrossRef]
3. Williams, S.W.; Martina, F.; Addison, A.C.; Ding, J.; Pardal, G.; Colegrove, P. Wire + Arc additive manufacturing. *Mater. Sci. Technol.* **2016**, *32*, 641–647. [CrossRef]
4. Martina, F.; Mehnen, J.; Williams, S.W.; Colegrove, P.; Wang, F. Investigation of the benefits of plasma deposition for the additive layer manufacture of Ti-6Al-4V. *J. Mater. Process. Technol.* **2012**, *212*, 1377–1386. [CrossRef]
5. Cong, B.; Ding, J.; Williams, S. Effect of arc mode in cold metal transfer process on porosity of additively manufactured Al-6.3%Cu alloy. *Int. J. Adv. Manuf. Technol.* **2015**, *76*, 1593–1606. [CrossRef]
6. Wu, B.; Pan, Z.; Ding, D.; Cuiuri, D.; Li, H.; Xu, J.; Norrish, J. A review of the wire arc additive manufacturing of metals: Properties, defects and quality improvement. *J. Manuf. Process.* **2018**, *35*, 127–139. [CrossRef]
7. Rodrigues, T.A.; Duarte, V.; Miranda, R.M.; Santos, T.G.; Oliveira, J.P. Current status and perspectives on wire and arc additive manufacturing (WAAM). *Materials* **2019**, *12*, 1121. [CrossRef]
8. Langelandsvik, G.; Grandcolas, M.; Skorpen, K.G.; Furu, T.; Akselsen, O.M.; Roven, H.J. Development of al-tic wire feedstock for additive manufacturing by metal screw extrusion. *Metals* **2020**, *10*, 1485. [CrossRef]
9. Garašić, I.; Štefok, M.; Jurica, M.; Skejić, D.; Perić, M. Mechanical Properties Analysis of WAAM Produced Wall Made from 6063 Alloy Using AC MIG Process. *Appl. Sci.* **2025**, *15*, 6740. [CrossRef]
10. Yu, Z.; Yuan, T.; Xu, M.; Zhang, H.; Jiang, X.; Chen, S. Microstructure and mechanical properties of Al-Zn-Mg-Cu alloy fabricated by wire + arc additive manufacturing. *J. Manuf. Process.* **2021**, *62*, 430–439. [CrossRef]
11. Gierth, M.; Henckell, P.; Ali, Y.; Scholl, J.; Bergmann, J.P. Wire Arc Additive Manufacturing (WAAM) of aluminum alloy AlMg5Mn with energy-reduced Gas Metal Arc Welding (GMAW). *Materials* **2020**, *13*, 2671. [CrossRef]
12. Omiyale, B.O.; Jack, T.A.; Ogedengbe, I.I.; Odeyemi, J.; Mishra, D.; Ogbeyemi, A.; Zhang, W.C. Impact of cold metal transfer variants on the mechanical and microstructural properties of aluminum alloys in wire arc additive manufacturing: A critical review. *Int. J. Adv. Manuf. Technol.* **2025**, *140*, 1183–1210. [CrossRef]
13. Akhavan, N.; Abbas, M.; Hanzaki, Z.; Moshiri, A.; Abbasi, A.; Reza, H. Heterogeneous microstructure enables strength—Ductility synergy in 2219 aluminium alloy fabricated by wire arc additive manufacturing (WAAM). *Prog. Addit. Manuf.* **2025**, *10*, 6437–6452. [CrossRef]
14. Pan, Y.; Guo, Z.; Li, X.; Wen, L. Influence of Heat Treatment on the Microstructure and Properties of 2319 Aluminum Alloy Produced by Wire Arc Additive Manufacturing. *Metals* **2025**, *15*, 1002. [CrossRef]
15. Ren, G.; Zheng, Y.; Xiong, R.; Zhao, C.; Wang, T.; Li, L. Effect of heat treatment on microstructure and corrosion behavior of AlCu alloy fabricated by wire arc additive manufacturing. *Mater. Charact.* **2024**, *218*, 114516. [CrossRef]
16. Wang, B.; Li, R.; Zhou, X.; Liu, F.; Wei, L.; Tian, L.; Song, X.; Tan, C. Insight into Role of Arc Torch Angle on Wire Arc Additive Manufacturing Characteristics of ZL205A Aluminum Alloy. *Materials* **2024**, *17*, 3771. [CrossRef] [PubMed]
17. Dinovitzer, M.; Chen, X.; Laliberte, J.; Huang, X.; Frei, H. Effect of wire and arc additive manufacturing (WAAM) process parameters on bead geometry and microstructure. *Addit. Manuf.* **2019**, *26*, 138–146. [CrossRef]
18. Bharat Kumar, C.H.; Anandakrishnan, V. Experimental investigations on the effect of wire arc additive manufacturing process parameters on the layer geometry of Inconel 825. *Mater. Today Proc.* **2020**, *21*, 622–627. [CrossRef]
19. Srinivas, M.N.; Manikandan, K.E.K.V.N. Parametric optimization and multiple regression modelling for fabrication of aluminium alloy thin plate using wire arc additive manufacturing. *Int. J. Interact. Des. Manuf.* **2022**. [CrossRef]
20. Yang, J.; Ni, Y.; Li, H.; Fang, X.; Lu, B. Heat Treatment Optimization of 2219 Aluminum Alloy Fabricated by Wire-Arc Additive Manufacturing. *Coatings* **2023**, *13*, 610. [CrossRef]
21. Kumar, A.; Maji, K. Selection of Process Parameters for Near-Net Shape Deposition in Wire Arc Additive Manufacturing by Genetic Algorithm. *J. Mater. Eng. Perform.* **2020**, *29*, 3334–3352. [CrossRef]
22. Panda, B.; Akhil, K.S.; Savalani, G.M.M. Evaluation of genetic programming-based models for simulating bead dimensions in wire and arc additive manufacturing. *J. Intell. Manuf.* **2019**, *30*, 809–820. [CrossRef]
23. Xia, C.; Pan, Z.; Polden, J.; Li, H.; Xu, Y.; Chen, S. Modelling and prediction of surface roughness in wire arc additive manufacturing using machine learning. *J. Intell. Manuf.* **2022**, *33*, 1467–1482. [CrossRef]
24. Barik, S.; Bhandari, R.; Mondal, M.K. Optimization of Wire Arc Additive Manufacturing Process Parameters for Low-Carbon Steel and Properties Prediction by Support Vector Regression Model. *Steel Res. Int.* **2024**, *95*, 2300369. [CrossRef]
25. Wacker, C.; Köhler, M.; David, M.; Aschersleben, F.; Gabriel, F.; Hensel, J.; Dilger, K.; Dröder, K. Geometry and Distortion Prediction of Multiple Layers for Wire Arc Additive Manufacturing with Artificial Neural Networks. *Appl. Sci.* **2021**, *11*, 4694. [CrossRef]
26. Irfan, M.; Fu, Y.; Singh, S.; Ullah, S.; Fazal, A.; Ibhadode, O.; Qureshi, A. Journal of Advanced Joining Processes Data-driven parameter optimization for bead geometry in wire arc additive manufacturing of 17-4 PH stainless steel. *J. Adv. Join. Process.* **2025**, *12*, 100319. [CrossRef]

27. Šket, K.; Brezočnik, M.; Karner, T.; Belšak, R.; Ficko, M.; Vuherer, T.; Gotlih, J. Predictive Modelling of Weld Bead Geometry in Wire Arc Additive Manufacturing. *J. Manuf. Mater. Process.* **2025**, *9*, 67. [CrossRef]
28. Rauch, M.; Nwankpa, U.V.; Hascoet, J.Y. Investigation of deposition strategy on wire and arc additive manufacturing of aluminium components. *J. Adv. Join. Process.* **2021**, *4*, 100074. [CrossRef]
29. Aldalur, E.; Veiga, F.; Suárez, A.; Bilbao, J.; Lamikiz, A. Analysis of the wall geometry with different strategies for high deposition wire arc additive manufacturing of mild steel. *Metals* **2020**, *10*, 892. [CrossRef]
30. Krolo, J.; Špada, V.; Bilušić, M.; Čatipović, N. Welding of Solid-State-Recycled Aluminum Alloy: Comparative Analysis of the Mechanical and Microstructural Properties. *Appl. Sci.* **2025**, *15*, 1222. [CrossRef]
31. *HRN EN ISO 6892-1:2019*; Metallic Materials—Tensile Testing—Part 1: Method of Test at Room Temperature (ISO 6892-1:2019; EN ISO 6892-1:2019). Croatia Standards Institute: Zagreb, Croatia, 2019. Available online: https://repozitorij.hzn.hr/norm/HRN+EN+ISO+6892-1:2019 (accessed on 1 November 2025).
32. Peko, I.; Marić, D.; Nedić, B.; Samardžić, I. Modeling and optimization of cut quality responses in plasma jet cutting of aluminium alloy EN AW-5083. *Materials* **2021**, *14*, 5559. [CrossRef]
33. Peko, I.; Čatipović, N.; Antunović, K.; Ljumović, P. Multi-Objective Optimization of Fatigue Performance in FDM-Printed PLA Biopolymer Using Grey Relational Method. *Sustainability* **2025**, *17*, 10902. [CrossRef]
34. Čatipović, N.; Peko, I.; Grgić, K.; Periša, K. Multi Response Modelling and Optimisation of Copper Content and Heat Treatment Parameters of ADI Alloys by Combined Regression Grey-Fuzzy Approach. *Metals* **2024**, *14*, 735. [CrossRef]
35. Peko, I.; Crnokić, B.; Čulić-Viskota, J.; Matić, T. Hybrid Grey–Fuzzy Approach for Optimizing Circular Quality Responses in Plasma Jet Manufacturing of Aluminum Alloy. *Appl. Sci.* **2025**, *15*, 7447. [CrossRef]
36. Köhler, M.; Hensel, J.; Dilger, K. Effects of thermal cycling on wire and arc additive manufacturing of al-5356 components. *Metals* **2020**, *10*, 952. [CrossRef]
37. Imširović, M.; Trdan, U.; Klobčar, D.; Bračun, D.; Nagode, A.; Berthe, L. Mitigating defects in directed energy deposited aluminium 5356 alloy through in-situ workpiece vibration. *J. Mater. Res. Technol.* **2024**, *33*, 1581–1599. [CrossRef]
38. Wieczorowski, M.; Pereira, A.; Carou, D.; Gapinski, B.; Ramírez, I. Characterization of 5356 Aluminum Walls Produced by Wire Arc Additive Manufacturing (WAAM). *Materials* **2023**, *16*, 2570. [CrossRef] [PubMed]
39. Oxford Alloys, Inc. Oxford Alloy® 5356. Available online: https://www.oxfordalloys.com/pdf/5356_Aluminum_97.pdf (accessed on 15 January 2026).
40. Hauser, T.; Reisch, R.T.; Breese, P.P.; Lutz, B.S.; Pantano, M.; Nalam, Y.; Bela, K.; Kamps, T.; Volpp, J.; Kaplan, A.F.H. Porosity in wire arc additive manufacturing of aluminium alloys. *Addit. Manuf.* **2021**, *41*, 101993. [CrossRef]
41. Arana, M.; Ukar, E.; Rodriguez, I.; Iturrioz, A.; Alvarez, P. Strategies to reduce porosity in Al-Mg WAAM parts and their impact on mechanical properties. *Metals* **2021**, *11*, 524. [CrossRef]

Disclaimer/Publisher's Note: The statements, opinions and data contained in all publications are solely those of the individual author(s) and contributor(s) and not of MDPI and/or the editor(s). MDPI and/or the editor(s) disclaim responsibility for any injury to people or property resulting from any ideas, methods, instructions or products referred to in the content.